Digital surface model generation over urban areas using high resolution satellite SAR imagery : tomographic techniques and their application to 3-Dchange monitoring

Martina Porfiri

ANNÉE 2016

THÈSE / UNIVERSITÉ DE RENNES 1
sous le sceau de l'Université Bretagne Loire

En Cotutelle Internationale avec
Université de Rome 1 « La Sapienza », Italie

pour le grade de

DOCTEUR DE L'UNIVERSITÉ DE RENNES 1

Mention : Traitement du signal et télécommunications

Ecole doctorale MATISSE

Martina Porfiri

Préparée à l'unité de recherche IETR, UMR CNRS 6164
Institut d'Electronique et de Télécommunications de Rennes
UFR ISTIC

Digital Surface Model generation over urban areas using high resolution satellite SAR imagery: tomographic techniques and their application to 3-D change monitoring

Thèse co-dirigée par :

Mattia CRESPI
Professeur, Université de Rome 1 « La Sapienza »
Laurent FERRO-FAMIL
Professeur, Université de Rennes 1

et soutenue à Rome le 26/07/2016

devant le jury composé de :

Riccardo LANARI
Directeur de Recherche, IREA-CNR, Italie, *examinateur*
Andreas REIGBER
Professeur, TU Berlin & DLR Munich, Allemagne, *rapporteur*
Stefano TEBALDINI
Maître de Conférences, Politecnico di Milano, Italie, *rapporteur*
Florence TUPIN
Professeur, TelecomParisTech, *rapporteur*

Be the change you want to see in the world

M. Gandhi

Contents

List of Figures

List of Tables

Glossary of acronyms

2D bi-dimensional 35

3D three-dimensional 8, 35, 47

4D four-dimensional 47

ABM Area Based Matching 39

AOI Area Of Interest 67, 69

CS Compressive Sensing 50

CSM COSMO-SkyMed 49

DEM Digital Elevation Model 35

DLR German Aerospace Center 29, 68

DOA Directions Of Arrival 58

DSM Digital Surface Model 8, 28, 35, 46, 47

DTM Digital Terrain Model 35

ESA European Space Agency 8

FIR Finite Impulse Response 59

GCPs Ground Control Points 38

GP Ground Point 38

GPS Global Positioning System 31

GSD Ground Sample Distance 8, 36

HS High Resolution Spotlight 67

InSAR Interferometric SAR 35

LCT Laser Communication Terminal 32

LS Least-Squares 37, 60, 61

MB MultiBaseline 48

MB-InSAR Multibaseline SAR Interferometric 10, 47, 49, 51, 54, 55

MB-PolInSAR Polarimetric MB-InSAR 54

MLRT Maximum-Likelihood Ratio Test 65

MOS Model Order Selection 63

MUSIC MUltiple SIgnal Classification 62

PolSAR Polarimetric SAR 75

PolTomSAR Polarimetric SAR Tomography 54

PSD Power Spectral Density 58

RAR Real Aperture Radar 16

RMSE Root Mean Square Error 28

RPCs Rational Polynomial Coefficients 37

RPFs Rational Polynomial Functions 37

SAR Synthetic Aperture Radar 8, 13

SNR Signal to Noise Ratio 28, 39

SP Single Polarization 49, 67, 74

SRTM Shuttle Radar Topography Mission 40

StereoSAR Radargrammetric SAR 35

TomoSAR Tomographic SAR 35, 51

TSX TerraSAR-X 49, 83

Résumé en français

La Terre est un système dynamique et sa surface est en constante évolution à différentes échelles de temps. L'imagerie satellitaire et les produits secondaires qui en dérivent jouent un rôle important en fournissant les informations nécessaires à l'analyse, au suivi et à la caractérisation de la dynamique de la surface de la Terre. Par conséquent, il est nécessaire d'obtenir des mesures rapides et précises de l'écosystème de la Terre. L'urbanisation et la gestion de l'environnement urbain et sa périphérie deviennent l'un des problèmes les plus cruciaux dans les pays développés et en voie de développement. Dans ces circonstances, les données de télédétection sont une source importante d'information qui reflète les interactions entre les êtres humains et leur environnement. Compte tenu de leur indépendance totale des contraintes logistiques sur le terrain, d'éclairage (lumière du jour) et de conditions météorologiques (nuages), les radars à synthèse d'ouverture (SAR) satellitaires peuvent fournir des contributions importantes d'environnements complexes à travers, par example, leur reconstruction 3-D. Les images SAR 2-D sont sujettes à d'importantes distorsions géométriques qui limitent fortement la portée de leur interprétation pour la caractérisation d'environnements complexes, comme les zones urbaines.
En particulier, à partir de 2007, la nouvelle génération de capteurs SAR à haute résolution comme l'italien COSMO-SkyMed, l'allemand TerraSAR-X et le canadien RADARSAT-

2 a permis d'acquérir des images SAR jusqu'à 1 m de résolution au sol en mode SpotLight et sous divers angle d'incidence. À l'heure actuelle l'attention se pote sur la récente famille de missions appelée Sentinel (-1 pour la technologie SAR) et développée par l'Agence Spatiale Européenne (ESA) spécifiquement pour les besoins opérationnels de Copernicus, le programme d'observation de la Terre dirigé par la Commission Européenne en partenariat avec l'ESA et visant à fournir des informations précises, pertinentes et facilement accessibles pour améliorer la gestion de l'environnement, comprendre et atténuer les effets du changement climatique et assurer une mission de sécurité civile. En effet, les capteurs et les technologies SAR modernes peuvent répondre à la demande publique concernant le suivi des changements rapides sur le terrain et dans les activités anthropiques. La possibilité de réaliser en temps quasi réel la cartographie 3-D de la surface de la Terre par satellite de télédétection représente un outil précieux pour plusieurs objectifs d'Horizon 2020, le nouveau programme-cadre pour la recherche et l'innovation en Europe.

Une des applications les plus importantes de la télédétection SAR est la génération de Modèles Numériques de Surface (DSM), qui permet de modéliser en trois dimensions la surface de la Terre. Dans les zones suburbaines et urbaines, en DSM se révèle très utile pour un grand nombre d'applications, qui incluent les calculs d'optimisation de l'emplacement des antennes de télécommunication, la cartographie des risques, la génération orthoimage, la planification urbaine et la surveillance. Trois techniques différentes imagerie SAR 3-D peuvent être discernées : le radargrammétrie, l'interférométrie et la tomographie. La radargrammétrie ne requiert en prin-

cipe que quelques images pour reconstruire la forme 3-D de la Terre, comme dans la vision stéréo humaine ou dans la photogrammétrie classique appliquée à l'imagerie optique, en exploitant uniquement l'information de signal d'amplitude. L'interférométrie utilise l'information de différence de phase entre (au moins) deux images SAR pour estimer l'élévation du terrain.

Ici, l'attention est mise sur la tomographie SAR : à partir d'une pile d'images recueillies en configuration interferometrique multibaselines, une telle technique permet d'extraire les informations de hauteur en formant une ouverture synthétique dans la direction d'élévation afin d'obtenir une résolution sensiblement améliorée. Les premières expériences importantes ont concerné l'analyse des structures de volume, comme les forêts, en utilisant des données aéroportés acquises à basse fréquence (par exemple les bandes L- ou P-). La première application SAR est présentée dans [54], a été obtenue en utilisant des données MultiBaseline en bande L acquises par E-SAR, le système aéroportée du DLR. Au fil des ans, différents articles ont été publiés sur la tomographie SAR appliquée à l'estimation de a la structure de la forêt [58, 31, 60], de l'épaisseur de la glace [59] ou la hauteur de bâtiments [70, 21, 30], pour résoudre les problèmes liés à la géométrie SAR , en particulier dans les zones urbaines complexes [7, 32, 53, 51].

Cette thèse de doctorat se concentre sur les potentialités élevées de techniques tomographiques pour la surveillance 3-D des changements et la caractérisation des zones complexes et denses bâties, en utilisant des estimateurs monodimensionnels de base comme Beamforming, Capon et MUSIC sur la zone urbaine de Paris en utilisant des données

TerraSAR-X à haute résolution et à polarisation unique. Le travail présenté ci-après limite le domaine des méthodes utilisées pour la reconstruction 3-D à des techniques d'estimation très rapides et n'aborde pas les estimateurs de signaux parcimonieux.

Dans un premier temps, l'analyse de la qualité interférométrique de l'ensemble de données transformées a été réalisée. Les résultats ont montré de bonnes valeurs de cohérence moyenne au sein de l'ensemble de la pile et ont permis de détecter des images considérées comme des valeurs aberrantes en termes de niveaux de conditions temporelles et spatiales, pour finalement sélectionner l'ensemble adéquat de données multitemporelles à traiter. L'extraction des tomogrammes a montré la capacité de distinguer plus d'un diffuseur à l'intérieur de la même cellule de résolution et de reconstituer la topographie de bâtiments. Successivement, une caractérisation tridimensionnelle globale a été réalisée dans le but de développer un outil de suivi des changements 3-D des structures simples. En outre, la possibilité de corriger les distorsions géométriques en raison de la projection en distance (qui affecte fortement ce genre de scénarios) et de déterminer les informations sur le nombre de diffuseurs (jusqu'à trois) et la réflectivité correspondant à l'intérieur d'une cellule de résolution ont été évalués. Plusieurs reconstructions 3D de structures simples ont été réalisées à la fois en terme de hauteurs des bâtiments et réflectivité verticale. Par ailleurs une analyse novatrice de la stabilité temporelle de la scène observée a été réalisée afin de détecter les diffuseurs stables et instables.

L'analyse effectuée en termes d'estimation de la réflectivité verticale a permis d'identifier différents comportements caractéristiques : des valeurs élevées sur l'interaction mur-sol a

révélé la présence de réflexion de type double rebond ; le sol étant caractérisé par de faibles valeurs de réflectivité. L'analyse de la stabilité dans le temps 3-D a démontré la possibilité de suivre l'évolution en 3-D en fonction du temps.
Finalement, il est possible d'affirmer que le traitement des données SAR haute résolution permet d'obtenir une forte amélioration en 3-D des capacités d'imagerie. Les reconstructions 3-D présentés dans cette thèse ont permis d'effectuer une caractérisation globale des zones urbaines à travers le traitement d'un ensemble adéquat d'images multitemporelles haute résolution SAR, démontrant ainsi les potentialités de la technique TomoSAR dans la correction des distorsions, dans la détermination des informations sur le nombre de diffuseurs et de la réflectivité correspondant à l'intérieur d'une cellule de résolution et leur évolution temporelle en utilisant des estimateurs mono-dimensionnels de base comme Beamforming, Capon et MUSIC.

Abstract

The Earth is a dynamic system and its surface is continuously changing at different time scales. Satellite imagery and derived secondary products play a relevant role in supplying the information necessary for analysing, monitoring and characterizing the Earth's surface dynamics. Accordingly, it is necessary to obtain timely and precise measurements of Earth's ecosystem. The urbanization and the management of urban environment and its periphery become one of the most crucial issues in developed and developing countries. In these circumstances, remote sensing data are an important source of information that reflects interactions between human beings and their environment. Given their complete independence from logistic constraints on the ground, illumination (daylight), and weather (clouds) conditions, Synthetic Aperture Radar (SAR) satellite systems may provide important contributions in complex environments 3-D reconstruction. SAR 2-D images are characterized by important geometric distortions, that severely limits their interpretation for the characterization of complex environments, such as urban areas.

In particular, starting from 2007 the new generation of high resolution Synthetic Aperture Radar (SAR) sensors as the Italian COSMO-SkyMed, the German TerraSAR-X and the Canadian RADARSAT-2 allowed to acquire SAR imagery up to 1 m Ground Sample Distance (GSD) in SpotLight mode,

and with different incidence angle. At the present the attention is on the recent new family of missions called Sentinels (-1 for SAR technology) and developed by the ESA specifically for the operational needs of Copernicus, the Earth observation programme headed by the European Commission in partnership with ESA and aimed to provide accurate, timely and easily accessible information to improve the management of the environment, understand and mitigate the effects of climate change and ensure civil security. Indeed, modern SAR sensors and technologies can satisfy the demand for the monitoring of rapid changes on the ground and in anthropic activities. The possibility of near-real-time 3D Earth surface mapping satellite remote sensing data enable the possibility of continuous observation of the Earth's surface, with short times of acquisitions and revisit, representing a valuable tool for several objectives of Horizon 2020, the new framework programme for research and innovation in Europe starting on 2014.

One of the most important applications of SAR remote sensing is the generation of Digital Surface Models (DSMs), that is, three-dimensional models of the Earth's surface. In suburban and urban areas it is very useful for a great number of applications, that include the inter-visibility calculations for the optimization of the location of telecommunication antennas, risk mapping, orthoimage generation, mission and urban planning and monitoring. Three different 3-D imaging techniques may be discerned: the radargrammetry, the interferometry and the tomography. Radargrammetry in principle requires just a couple of images to reconstruct the 3-D shape of the Earth, like in the human stereo vision or in the classical photogrammetry applied to optical imagery, exploiting

just the amplitude signal information. Interferometry uses the phase differences information between (at least) two SAR images to lead the terrain elevation.

Here the attention is put on the SAR Tomography: starting from a stack of images collected using multibaseline data performed in interferometric configuration, such a technique allows to retrieve height information forming a synthetic aperture in the elevation direction in order to achieve a substantially improved resolution. First important experiments has concerned the analysis of volume structures, such as forests, using low frequencies (e.g. L- or P-band) airborne sensors. The first application is represented by [56]. The experimental results have been achieved using MultiBaseline L-band data sets acquired by the DLR's E-SAR (airborne) system. Succesevely, over the years, different papers have been published about the tomographic SAR techniques application in order to retrieve the forest structure [60, 33, 62], to estime ice thickness [61] or building height [70, 23, 32], to solve the layover problem induced by strong terrain slopes or discontinuities in the imaged scene, especially in complex urban areas [9, 34, 55, 53].

The present PhD thesis is focused on the high potentialities of tomographic techniques in 3-D change monitoring and characterization for complex and dense built-up areas using basic mono-dimensional estimators as Beamforming, Capon and MUSIC combined to very high satellite SAR resolution imagery. 2-D and 3-D analysis have been presented over the urban area of Paris using TerraSAR-X data at high resolution and single polarisation. The present work is mainly focused on the 3-D reconstruction by very fast estimation techniques and does not take into account parsimonious signal estima-

tors.

At first, the analysis of the interferometric quality of the processed data set has been performed. The results showed good mean coherence values within the entire stack and allowed to detect images considered as outlier in terms of temporal and spatial baselines and to select the adequate set of multitemporal data to be processed. The extraction of 2-D tomograms over different azimuth-profile has showed the capabilities to distinguish more than one scatterer within the same resolution cell and to reconstruct the vertical building profiles. Successively, a global three-dimensional characterization has been performed in order to develop a monitoring tool for the 3-D changes of single structures. Moreover, the possibility to correct the geometric distortions due to the layover (that strongly affects such kind of scenarios) and to determine the information about the number of scatterers (up to three) and the corresponding reflectivity within one resolution cell have been evaluated. Several 3-D reconstructions of single structures have been performed both in term of buildings heights and vertical reflectivity. Moreover an innovative time stability analysis of the observed scene have been carried out in order to detect the stable and unstable scatterers.

The analysis performed in terms of vertical reflectivity estimation allowed to identify different features behaviour: high values at the interaction wall-ground revealed the double bounce strong reflection occurring in that area; the ground is characterized by low reflectivity values. The 3-D time stability analysis demonstrated the possibility to monitor the 3-D change depending on the time.

Eventually, it is possible to assert that processing high resolution SAR data allows to achieve a strong improvement in

3-D imaging capabilities. The 3-D reconstructions presented in the present thesis enabled to perform a global characterization of build-up areas, processing an adequate set of multitemporal high resolution SAR images. It has been demonstrated the potentialities of TomoSAR technique in distortions correction, in determining information about the number of scatterers and the corresponding reflectivity within one resolution cell and in 3-D change monitoring using basic mono-dimensional estimators as Beamforming, Capon and MUSIC.

Chapter 1

Introduction

Nowadays our life is strongly dependent on satellites in orbit around the Earth which make us safer, provide modern conveniences, broadcast entertainment, information about our planet gathered from space and sent around the globe in the blink of an eye.
First satellite space programs have been run with military purposes and the first images of the Earth were captured in the 1960s, even though its capabilities have not been immediately understood. Indeed with respect to that date, the impact of this information on our everyday life is only a recent phenomenon. It was during the past decade (since 1999, with the launch of IKONOS) that a kind of competition started among different companies and agencies to launch optical and radar sensors with higher and higher resolution for civilian applications. Accordingly, many research groups around the world started to develop methodological and practical investigations about the large number of applications of this new satellite imagery, such as land monitoring, archaeological and environmental studies, cartography and mapping. It was clearly understood that high resolution sensors permit an easier acquisition of data of the same area at regular intervals, which is useful to monitor natural and anthropic phenomena evolving in time (e.g., urban growth, natural disasters); moreover, high resolution remote sensors allow us to obtain

images of areas where it may be difficult to carry out traditional surveys for logistic reasons (e.g., developing countries, wild and remote areas). After many traditional optic sensors, radar ones acquired importance in recent years due to their improving acquisition resolution and their capacity to acquire imagery in situation where optical sensors are less useful: thanks to their active sensor nature and spectral domain they are able to acquire imagery through clouds and even during night. In particular, starting from 2007 the new generation of high resolution Synthetic Aperture Radar (SAR) sensors as the Italian COSMO-SkyMed, the German TerraSAR-X and the Canadian RADARSAT-2 allowed to acquire SAR images up to 1 m Ground Sample Distance (GSD) in SpotLight mode, and with different incidence angles. At the present the attention is on the recent new family of missions called Sentinels (-1 for SAR technology) and developed by the European Space Agency (ESA) specifically for the operational needs of Copernicus, the Earth observation programme headed by the European Commission in partnership with ESA and aimed to provide accurate, timely and easily accessible information to improve the management of the environment, understand and mitigate the effects of climate change and ensure civil security. Indeed, modern SAR sensors and technologies can satisfy the demand for the monitoring of rapid changes on the ground and in anthropic activities. The possibility of near-real-time three-dimensional (3D) Earth surface mapping satellite remote sensing data enable the possibility of continuous observation of the Earth's surface, with short times of acquisitions and revisit, representing a valuable tool for several objectives of Horizon 2020, the new framework programme for research and innovation in Europe starting on 2014.

One of the most important applications of SAR remote sensing is the generation of Digital Surface Model (DSM), that is, three-dimensional models of the Earth's surface. In modern map production, the 3-D imaging techniques have become an information source for scene analysis and

understanding, for change detection, for GIS database updating, for cartographic 3-D feature extraction and reconstruction. In suburban and urban areas it is very useful for a great number of applications, that include the inter-visibility calculations for the optimization of the location of telecommunication antennas, risk mapping, orthoimage generation, mission and urban planning. Starting from the SAR data, with respect to the requirements of data accuracy and completeness and of realization efficiency and versatility, three different 3-D imaging techniques may be discerned: radargrammetry, interferometry and tomography.
Radargrammetry in principle requires just a couple of images to reconstruct the 3-D shape of the Earth, like in the human stereo vision or in the classical photogrammetry applied to optical imagery, exploiting just the amplitude signal information. Interferometry uses the phase differences information between (at least) two SAR images to lead the terrain elevation. Tomography represents an evolution of the last one, performing a 3-D imaging by the formation of an additional synthetic aperture in elevation using more than two SAR acquisitions performed in interferometric configuration.

1.1 Research objectives

The present PhD thesis is focused on the analysis of dense and complex urban areas by means of tomographic techniques applied to high resolution satellite SAR imagery. Starting from the classical second product of this approach, that is the reflectivity two-dimensional tomograms, a global three-dimensional characterization has been performed in order to develop a monitoring tool for the 3-D changes of single structures. Moreover, the possibility to correct the geometric distortions due to the layover (that strongly affects such kind of scenarios) and to determine the information about the number of scatterers (up to three) and the

corresponding reflectivity within one resolution cell have been evaluated. Several 3-D reconstructions of single structures have been performed both in terms of buildings heights and vertical reflectivity. Moreover an innovative time stability analysis of the observed scene have been carried out in order to detect the stable and unstable scatterers. The processing have been performed using an adequate high resolution Multibaseline SAR Interferometric (MB-InSAR) data acquired over Paris urban area by the satellite TerraSAR-X. The final goal is to demonstrate the high potentialities of tomographic techniques in 3-D change monitoring and characterization for built-up areas using basic mono-dimensional estimators as Beamforming, Capon and MUSIC combined to very high satellite resolution data. The present work is mainly focused on the 3-D reconstruction by very fast estimation techniques and does not take into account parsimonious signal estimators.
Starting from these purposes, the thesis is structured in the following chapters:

- **CHAPTER 2**: introduction and description of SAR imaging principles (acquisition mode, geometric distortion, speckle noise) and satellite platforms, with particular attention for TerraSAR-X

- **CHAPTER 3**: overview of the three SAR 3-D imaging techniques: radargrammetry, interferometry and tomography

- **CHAPTER 4**: examination of the tomographic focusing technique, including the basic principles and the state of the art for the urban analysis

- **CHAPTER 5**: description of the data set, analysis of the data interferometric quality and of the 2-D experimental results obtained using the Beamforming, Capon and MUSIC spectral estimation techniques

- **CHAPTER 6**: analysis of the 3-D experimental results in terms of building height retrieval, vertical reflectivity estimation and time stability analysis
- **CHAPTER 7**: conclusions and perspectives

Chapter 2

SAR: Synthetic Aperture Radar

SAR possesses some unique characteristics, such as all-weather functionality, capability of penetrating dense cover, and signal coherence, that gives it a considerable advantage over other infrared or optical sensors. Remote sensing is the science of obtaining and interpreting information from a distant point of view, using sensors that are not in physical contact with the object being observed [47]. The science of remote sensing in its broadest sense includes aerial, satellite, and spacecraft observations of the surfaces and atmospheres of the planets in our solar system, though the Earth is obviously the most frequent target of study. The term is customarily restricted to methods that detect and measure electromagnetic energy (see Fig. 2.1).

Imagery acquired by airborne or satellite sensors provides an important source of information for mapping and monitoring natural and manmade features on the land surface. The spatial, spectral, and temporal components of an image or set of images all provide information that we can use to form interpretations about surface materials and conditions. For each of these properties we can define the resolution of the images produced by the sensor system. These image resolution factors place limits on which information we can derive from remotely sensed images.

The *spatial resolution* is the smallest distance separating two objects

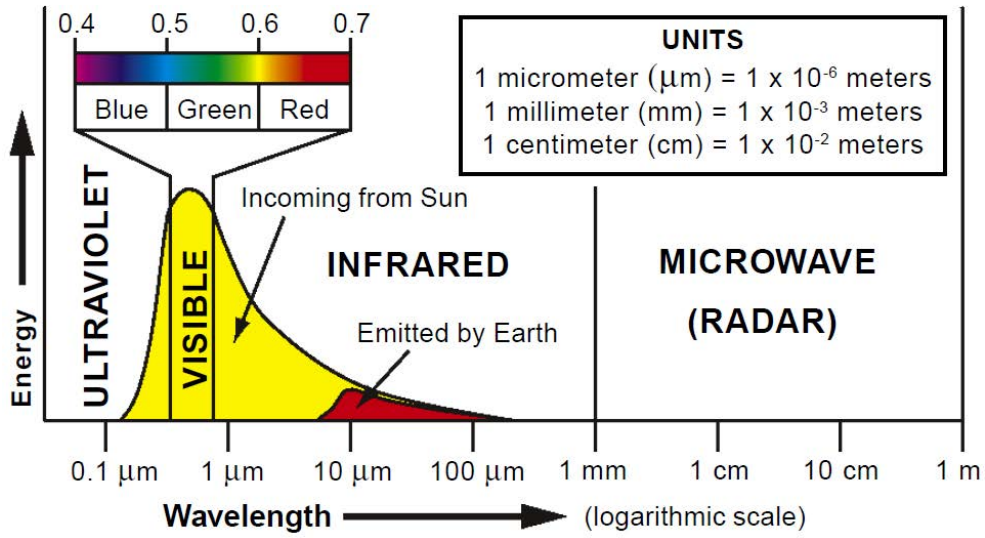

Fig. 2.1 – Electromagnetic spectrum

that can be discerned. It is a measure of the spatial detail in an image, which is a function of the design of the sensor and its operating altitude above the Earth's surface. Each of the detectors in a remote sensor measures energy received from a finite patch of the ground surface. The smaller these individual patches are, the more detailed will be the spatial information that we can interpret from the image. For digital images, spatial resolution is most commonly expressed as the ground dimensions of an image cell.

The *spectral resolution* of a remote sensing system can be described as its ability to distinguish different parts of the range of measured wavelengths. In essence, this amounts to the number of wavelength intervals (bands) that are measured, and how narrow each interval is. An image produced by a sensor system can consist of one very broad wavelength band, a few broad bands, or many narrow wavelength bands. The names usually used for these three image categories are panchromatic, multispectral, and hyperspectral, respectively.

The surface environment of the Earth is dynamic, with change oc-

curring on time scales ranging from seconds to decades or longer. The seasonal cycle of plant growth that affects both natural ecosystems and crops is an important example. Repeat imagery of the same area through the growing season adds to our ability to recognize and distinguish plant or crop types. A time-series of images can also be used to monitor changes in surface features due to other natural processes or human activity. The time-interval separating successive images in such a series can be considered to define the *temporal resolution* of the image sequence.

Satellites detect the signal on several wavelengths depending on their spectral and spatial characteristics. Then, also the data resolution depends on these characteristics, how it is shown in table 2.1

Type	Satellite	Spectral Resolution	Temporal Resolution	Best Spatial Resolution (rg x az)
OPTICAL	WorldView-3	29 bands (400-2245 nm)	< 1 days	0.31x0.31 m (panchromatic at nadir)
	IKONOS	5 bands (450-900 nm)	3 days	0.82x0.82 m (panchromatic at nadir)
	Sentinel-2	13 bands (443-2190 nm)	at equator 10 days (1 sat) - 5 days (all sat)	10x10 m (4 visible, near-infrared)
RADAR	TerraSAR-X	Microwave (X band)	2.5-11 days (depending on imaging mode)	0.6x0.24 m (Staring SpotLight mode)
	Sentinel-1	Microwave (C band)	12 days (1 sat) - 6 days (all sat)	5x5 m (StripMap mode)
	ALOS-2	Microwave (L band)	14 days	3x1 m (Spotlight mode)

Table 2.1 – Platform analysis at different scale of interest

In comparison with the optical remote sensing, the radar remote sensing offers some advantages, such as:

- all weather capability (small sensitivity of clouds, light rain)
- day and night operation (independence of sun illumination, i.e. active system)
- sensitivity to dielectric properties (water content , biomass, ice)
- sensitivity to surface roughness (ocean wind speed) and to dielectric properties (water content, biomass, ice)
- accurate distance measurements
- sensitivity to man made objects

- subsurface penetration (the longer the wavelength, the higher the transmission through a medium)

and some inconveniences, such as:

- complex interactions (difficulty in understanding, complex processing)
- speckle noise effects
- distortion of a scene geometry

2.1 SAR principles

In this section a basic introduction of SAR principles is given, from the fundamentals of the system to the main sensor features. Since during the last decades this technology has been deeply described and investigated, here only the concepts useful for understanding the present thesis are presented. For detailed discussions one can refer to, e.g., [15, 25].
Imaging radar is an active illumination system. An antenna, mounted on a platform, transmits a radar signal in a side-looking direction towards the Earth's surface. The reflected signal, known as the echo, is backscattered from the surface and received a fraction of a second later at the same antenna (monostatic radar) (see Fig. 2.2). For coherent radar systems such as SAR, the amplitude and the phase of the received echo (which are used during the focusing process to construct the image) are recorded. Aperture means the opening used to collect the reflected energy that is used to form an image. In the case of radar imaging this is the antenna. For Real Aperture Radar (RAR) systems, only the amplitude of each echo return is measured and processed. The spatial resolution of RAR is primarily determined by the size of the antenna used: the larger the antenna, the better the spatial resolution. The spatial resolution can be defined through to directions: *slant range direction*, perpendicular to

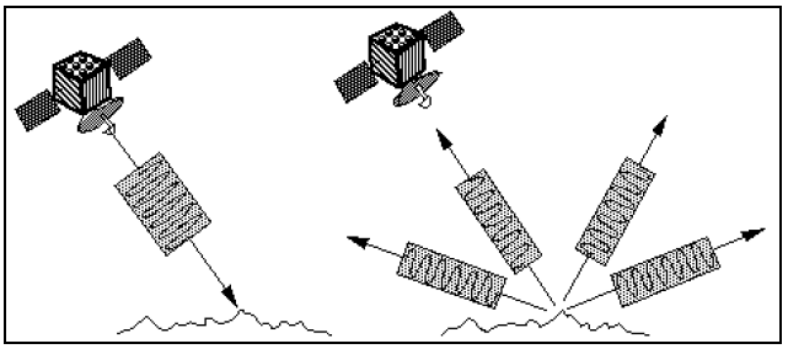

Fig. 2.2 – Signal trasmitted from the satellite (left image) and signal backscattered from the surface (right image)

flight path of the spacecraft, and *azimuth direction*, parallel to the flight path of the spacecraft (see Fig. 2.3). Note that, defining the *range* as the distance from the radar to the scatterer, the *slant range* is the dimension in the image, different to the *ground range* that is the dimension along the ground. Another important element is the *look angle* θ (or *off-nadir angle*), defined as the vertical angle between the inclination of the antenna and the nadir. The look angle is steepest for the portion of the image nearest the flight path (near range), and decreases toward the far range. The *range resolution* Δr (see Fig. 2.4a) is defined for unmodulated pulses as:

$$\Delta r = \frac{c\tau}{2} \tag{2.1}$$

where:

- c is the speed of light in vacuum
- τ is the pulse duration

Range resolution is independent of the height of the spacecraft H, and it depends primarily on the duration of the pulse τ. For modulated pulse, with bandwidth B, the range resolution is given by

$$\Delta r = \frac{c}{2B} \tag{2.2}$$

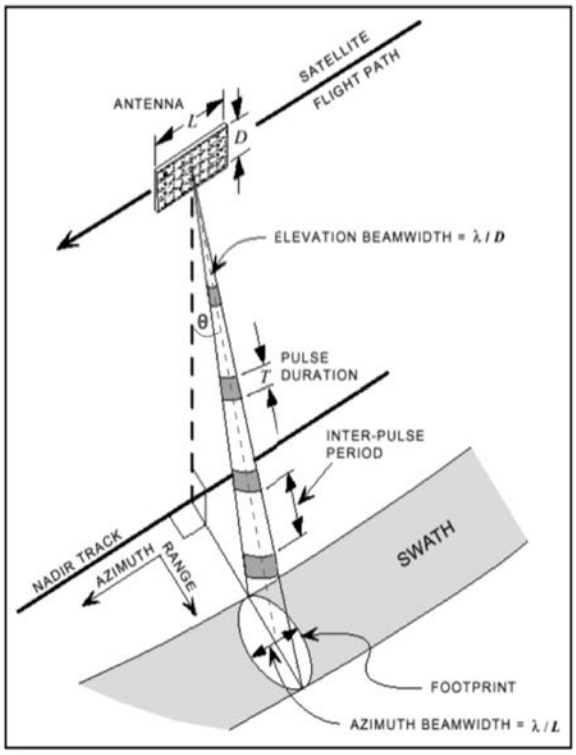

Fig. 2.3 – RAR system from a satellite

The *azimuth resolution* Δa (see Fig. 2.4b) may be approximated as:

$$\Delta a = \frac{R\lambda}{L} \tag{2.3}$$

where:

- R is the slant range
- λ is the wavelength of the microwave
- L is the length of the aperture of radar antenna

Azimuth resolution is dependent also on the height of the spacecraft H, and it improves (Δa reduces) as the antenna length L is increased. The radar image is arranged by a pixel matrix, in which each pixel is

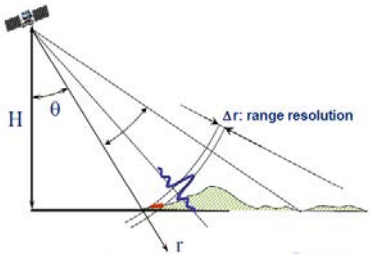

(a) Slant range resolution

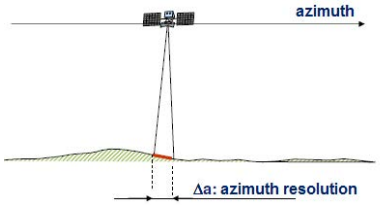

(b) Azimuth resolution

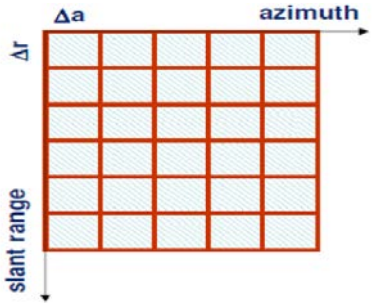

(c) Cell resolution

Fig. 2.4 – Image resolution

associated to a resolution cell (see Fig. 2.4c).

To improve the resolution of radar images, SAR was developed in the 1960s. The SAR systems take advantage of the Doppler history of the radar echoes generated by the forward motion of the spacecraft to synthesise a large antenna (see Fig. 2.5). This allows high azimuth resolution in the resulting image despite a physically small antenna (L is drastically reduced). As the radar moves, a pulse is transmitted at each position. The return echoes pass through the receiver and are recorded in an echo store. SAR requires a complex integrated array of onboard navigational and control systems, with location accuracy provided by both Doppler and inertial navigation equipment. For sensors such as ERS-1/2 SAR and ENVISAT ASAR, orbiting about 900km from the Earth, the area on the ground covered by a single transmitted pulse (footprint) is about 5 km long in the along-track (azimuth) direction.

SAR processing is a complicated data processing of received signals

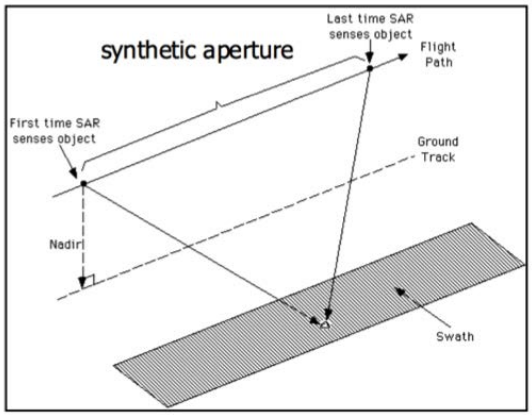

Fig. 2.5 – Sbaceborne SAR system [1]

and phases from moving targets with a small antenna, the effect of which is to should be theoretically convert to the effect of a large antenna, that is a synthetic aperture length, i.e. the beam width by range which a RAR of the same length, can project in the azimuth direction. Compared to the RAR azimuth resolution described earlier, the azimuth resolution Δa of the SAR is much improved, that is:

$$\Delta a = \frac{L}{2} \tag{2.4}$$

Indeed, it means that the azimuth resolution Δa of a SAR is only determined by the length of the real aperture of an antenna L, independently of the slant range R. Each pixel of the SAR image holds the sum of the backscattered echoes toward the radar from all the objects in the resolution cell. The signal intensity received by the radar depends on the object in the resolution cell, e.g. urban or rocky areas have high intensity (white pixel), vegetated areas have medium intensity (grey pixel) and smooth areas (as basins of calm water) have low intensity (black pixel)(see Fig. 2.6). Diverse scattering mechanisms can be associated to these different media. For example double bounce reflection can occur between the ground and building façades as well as between the ground

and under-foliage objects and between the object and the trunk, the volumic scattering is often related to the presence of vegetated (canopy) areas, the single bounce is derived from the building roof or the bare soil.

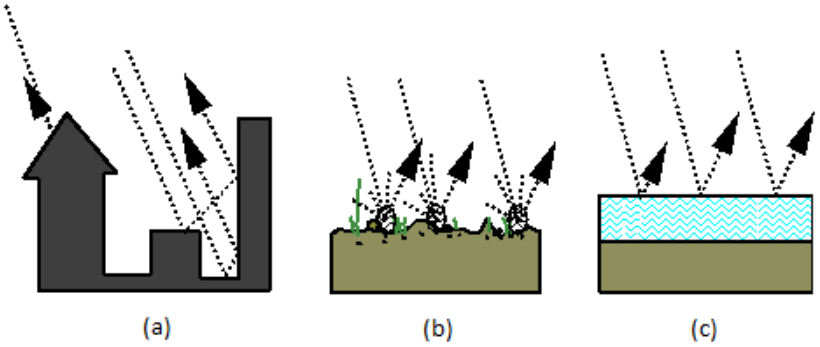

Fig. 2.6 – Different backscatters from (a) an urban area, (b) a vegetated area, (c) a smooth areas

SAR images contain a coherent, amplitude and phase, information. Depending on the information exploited for 3-D mapping, two techniques may be discerned: interferometry based on phase and radargrammetry based on amplitude. The main difference between these two techniques is that radargrammetry calculates the image range offset using the position matching of the same ground targets in two images whereas InSAR calculates the phase difference between two images.
SAR imaging operating modes are:

- *Spotlight Mode*, in which the antenna is steered (both in the azimuth and the elevation plane) during the overall acquisition time in order to illuminate the required scene for a time period longer than the one of the standard strip side view, increasing the length of the synthetic antenna and therefore the azimuth resolution (at expense of the azimuth coverage). In such configuration the acquisition is performed in frame mode, hence it is limited in the azimuth direction due to the technical constraints deriving from

the azimuth antenna pointing. The implementation allowed for this acquisition mode is the Enhanced Spotlight. In the Enhanced Spotlight mode, the spot extension is achieved by a antenna electronic steering scheme requiring the centre of the beam steering to be located beyond the centre of the imaged spot, thus increasing the observed Doppler bandwidth for each target

- *Stripmap Mode*, which is the most common imaging mode (e.g. similar to ERS mission one), obtained by pointing the antenna along a fixed direction with respect to the flight platform path. The antenna footprint covers a strip on the illuminated surfaces as the platform moves and the system operates. The acquisition is virtually unlimited in the azimuth direction, except for the limitations deriving from the SAR instrument duty cycle

- *ScanSAR Mode*, which allows larger swath in range with respect to the Stripmap one, but with a less spatial resolution, obtained by periodically stepping the antenna beam to neighbouring subswaths. Since only a part of the synthetic antenna length is available in azimuth, the azimuth resolution is hence reduced. In such configuration the acquisition is performed in adjacent strip mode, hence it is virtually unlimited in the azimuth direction, but for the limitations deriving from the SAR instrument duty cycle

2.2 SAR effects

2.2.1 Radar geometric distortions

The SAR system measures the time delay between transmission and reception of a pulse in order to determine where targets are relative to one another in the range direction. Consequently, the SAR systems are range-based. This leads to geometric distortions due to relief displace-

ment, such as *foreshortening*, *layover*, *shadow*, that decrease the reliability of radar imageries (see Fig. 2.7).

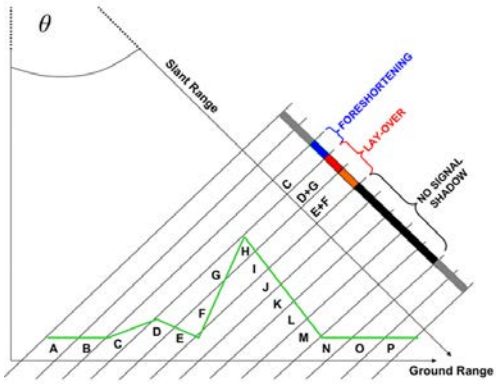

Fig. 2.7 – Radar geometric distortions: foreshortening, layover and shadow

Consider the mountain as sketched in the Fig. 2.8.

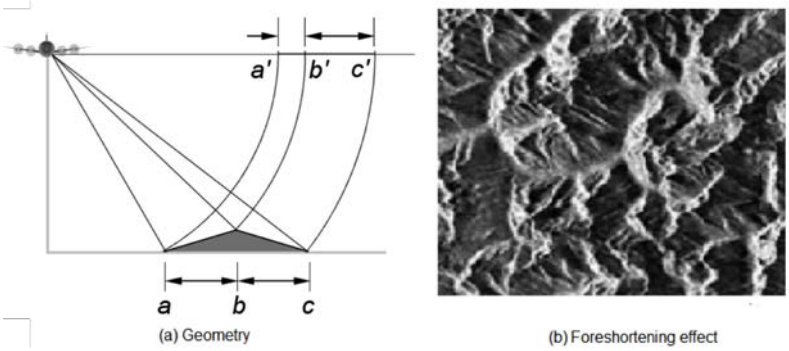

Fig. 2.8 – Foreshortening [5]

Points A, B and C are equally spaced when vertically projected on the ground (as it is done in conventional cartography). However, the distance $\overline{A'B'}$ is considerably shortened compared to $\overline{B'C'}$, because the top of the mountain is relatively close to the SAR sensor. Also note that $\overline{BC}$, the backslope becoming $\overline{B'C'}$ is consequently stretched. *Foreshortening* is a quite common effect in SAR images of mountainous areas.

Especially in the case of steep-looking spaceborne sensors, the across-track slant-range differences between two points located on foreslopes of mountains are smaller than they would be in flat areas. This effect results in an across-track compression of the radiometric information backscattered from foreslope areas which may be compensated during the geocoding process if a terrain model is available. Foreshortening is obvious in mountainous areas (top left corner), where the mountains seem to 'lean' towards the sensor. Foreshortening effects are greatest in the near range (closer to the transmitter and receiver) and less pronounced in the far range. The lighter edges are the slopes facing the radar system. The narrow bright slopes (AB) illustrate increased compression in the near range.

If, in the case of a very steep slope, targets in the valley points of mountains have a larger slant range than the mountain top, then the foreslope is reversed in the slant range image (see Fig. 2.9). This phe-

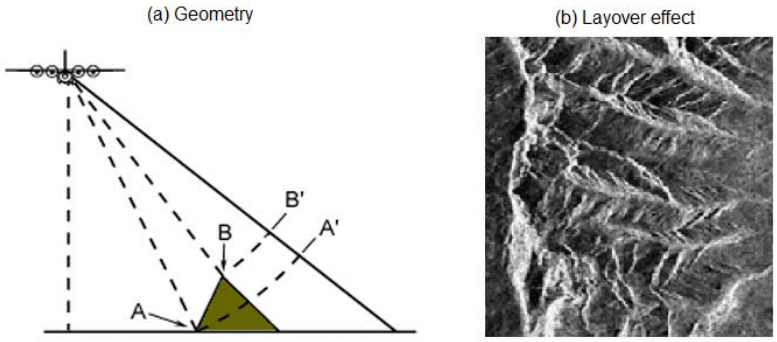

Fig. 2.9 – Layover in case of very steep slope [3]

nomenon is called *layover*: the ordering of surface elements on the radar image is the reverse of the ordering on the ground. Generally, these layover zones, facing radar illumination, appear as bright features on the image due to the low incidence angle. Ambiguity occurs between targets hit in the valley and in the foreslope of the mountain, in case they have the same slant-range distance. For steep incidence angles this might also

include targets on the backslope. Geocoding cannot resolve the ambiguities due to the representation of several points on the ground by one single point on the image; these zones also appear bright on the geocoded image. In built-up areas this phenomenon occurs at locations with steep elevation gradient facing towards the sensor, e.g. tall buildings. In Fig. 2.10a the layover effect is represented: different backscatters, e.g. the roof, the wall and the ground, are imaged in the same resolution cell. This causes a scattering ambiguity problem along the vertical direction that, generally, can be solved by SAR tomographic techniques (see chapter 4). An example of the layover effect is depicted in Fig. 2.10b where the well-known Tour Eiffel (captured by the satellite TerraSAR-X) is imaged 'laying down' onto the ground along the range direction (one may also note the Tower's shadow over the bottom of the figure).

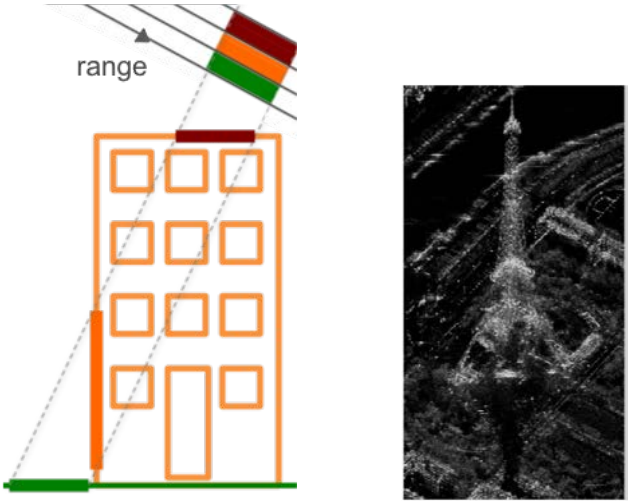

(a) (b)

Fig. 2.10 – (a) Layover and shadow phenomena in built-up areas; (b) TerraSAR-X image captured in Spotlight mode (image taken from [7])

A slope away from the radar illumination with an angle that is steeper than the sensor depression angle causes *radar shadows* (see Fig. 2.10a and Fig. 2.11).

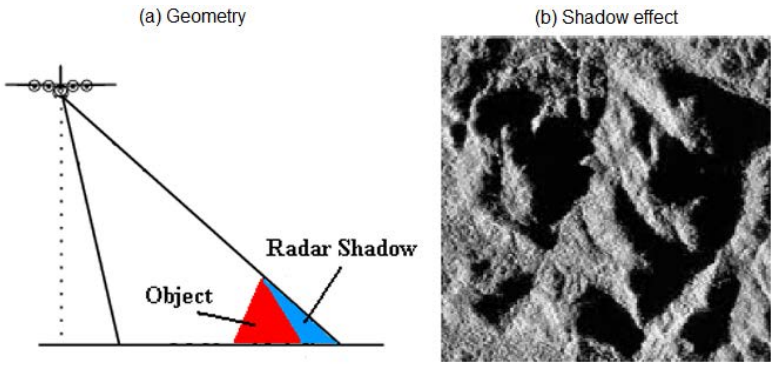

Fig. 2.11 – Shadow [3]

Shadow regions appear as dark (zero signal) with any changes due solely to system noise, sidelobes, and other effects normally of small importance. It should be also noted that the radar shadows of two objects of the same height are longer in the far range than in the near range.

2.2.2 Speckle noise

Speckle is a granular noise (see Fig. 2.12a) that inherently exists in all types of coherent imaging systems such as SAR imagery. This extremely complex pattern bears no obvious relationship to the macroscopic properties of the object illuminated. Rather it appears chaotic and unordered, and is best described quantitatively by the methods of probability and statistics [66]. Unlike system noise (additive noise), speckle is an electromagnetic effect. Considering its statistical fluctuations, speckle may be modeled by a multiplicative gaussian noise in SAR images. It is coherent interference of waves scattered from terrain elements observed in each resolution cell. The vast majority of surfaces, synthetic or natural, are extremely rough on the scale of an optical wavelength [28]. Under illumination by coherent light, the wave reflected from such a surface consists of contributions from many independent scattering areas. Propagation of this reflected light to a distant observation point results in the addition

of these various scattered components with relative delays which may vary from several to many wavelengths, depending on the microscopic surface and the geometry. Consequently, when illuminated by the SAR, each target contributes backscatter energy which, along with phase and power changes, is then coherently summed for all scatterers, so called random-walk (see Fig. 2.12b). The SAR focusing operation coherently combines the received signals to form the image. The scattered wave phase addition results in both constructive and destructive interference of individual scattered returns and randomly modulates the strength of the signal in each resolution cell.

The presence of speckle in an image reduces the resolution of the image

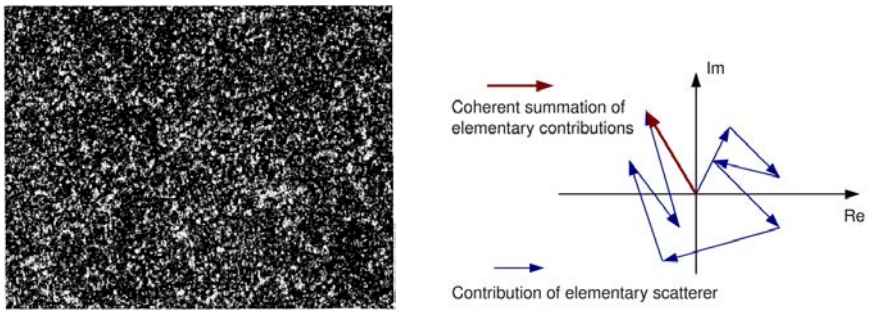

(a) Typical speckle pattern (b) Random-walk of several scatters

Fig. 2.12 – Speckle effects

and the detectability of the target. The ideal speckle reduction filter should reduce speckle with minimum loss of information as in homogeneous area, preserving radiometric information and edges between different areas, as in textured areas, preserving radiometric information and spatial signal variability. Reducing the effect of speckle noise enhances radiometric resolution (better discrimination of scene targets and easier automatic image segmentation) at the expense of spatial resolution. Most of speckle reduction techniques have been studied by researchers, and the filtering is one of the common methods which is used to reduce the speckle noises. The process used to apply filters to an image is known

as convolution, and may be applied in either the spatial [44, 42, 38] or frequency domain [68, 36].
The influence of the preprocessing speckle filtering algorithms on the DSM generation has been taken into account, e.g., in [43, 52, 64]. More thoroughly, in [52] its impact within the radargrammetric SAR processing chain (see section 3.1) has been studied considering the possibility to identify a greater number of homologous points characterised by a better Root Mean Square Error (RMSE) value. The work has led to infer that the speckle filtering algorithms allow to match a greater number of points, unfortunately characterizing by a lower accuracy value. This is caused by the presence of low accuracy points that alter the data and the final results. Furthermore, the relationship between the Signal to Noise Ratio (SNR) signal value and the elevation data statistics has been underlined, introducing the concept that the low accuracy points could be discarded by dynamically changing the SNR threshold value during the image matching procedure (see 3.1).

2.3 SAR platforms: TerraSAR-X

Sensors based in space are used for Earth observation, be it for research into the alterations taking place in our atmosphere, for climate research, for the monitoring of processes in our oceans, for geological investigations, and much more besides. Remote sensing data obtained from space thus complement and complete Earth-based measurements. They are always essential if a global view of our Earth is required, as is the case, for example, with the weather, or with the monitoring of the polar ice caps. With the TerraSAR-X radar satellite, the land masses of the Earth are particularly closely inspected. This includes the mapping of our forests, the generation and current updating of land utilization maps, the recording of derelict land areas and the estimation of the maturity level of areas in agricultural use, as well as the study and monitoring of geologically

active areas such as volcanic and earthquake regions. With the increasing technical capability of these sensors this kind of data can be extracted from satellites with ever more precision.

TerraSAR-X is Germany's first national remote sensing satellite that has been implemented in a public-private partnership between the German Aerospace Center (DLR) and EADS Astrium GmbH, with a significant financial participation from the industrial partner. It is designed to satisfy the steadily growing demand of the private sector for remote sensing data in the commercial market. As mentioned, TerraSAR-X products can be used for a variety of applications. Moreover, the first experimental data acquisitions have been successfully completed, among them data takes in the so-called Dual-Receive Antenna Mode, which allows motion measurements as well as fully polarimetric data acquisitions. In addition, the so-called TOPS-Mode could be demonstrated for the first time, a new method for imaging particularly wide swathes with high quality.

Today it is difficult to imagine our life without satellites. Whether the daily weather report using meteorological satellites, the live transmission of an ongoing event from remote areas using modern communication satellites or the navigation of ships on the world's oceans by means of global positioning satellites: these services that in recent times have become part of our daily life are only possible thanks to technologically advanced missions operating in space.

With TerraSAR-X it is used the Synthetic Aperture Radar sensor (see p. 15). This contributes significantly to the reliability of the system, a property that is increasingly requested by many users, since data are often required at a certain point in time. Today, these kinds of capabilities are no longer just of interest for scientific applications; such data are also being asked for increasingly on the commercial market. This is the reason why TerraSAR-X, Germany's first national remote sensing satellite, has been implemented in a so-called public-private partnership between the German Aerospace Center and EADS Astrium GmbH.

The different kinds of imagery which can be acquired by TERRASAR-X are the following one [6]:

- Staring SpotLight (ST): 0.6x0.24 m rg/az resolution, 4x3.7 km rg/az scene size
- HighRes SpotLight 300 MHz (HS300): 0.6x1.1 m rg/az resolution, 10x5 km rg/az scene size
- HighRes SpotLight (HS): up to 1.2x1.1 m rg/az resolution, 10x5 km rg/az scene size
- SpotLight (SL): up to 1.2x1.7 m rg/az resolution, 10x10 km rg/az scene size
- StripMap (SM): up to 1.2x3.3 m rg/az resolution, 30x50 km rg/az scene size
- ScanSAR (SC): 1.2x18.5 m rg/az resolution, 100x150 km rg/az scene size
- Wide ScanSAR (WS): up to 1.7x40 m rg/az resolution, 270x200 km rg/az scene size

In Table 2.2 are showed the main TerraSAR-X technical data. The TerraSAR-X satellite pictorial representation is given in Fig. 2.13.

The data recorded by the SAR instrument are transferred via a downlink antenna to the ground receiving station. The antenna is secured to a 3.3 meters long mast in order to avoid interferences caused by the radar antenna. The mast is folded up during the launch and is only extended after positioning of the satellite into its orbit. It allows simultaneous acquisition of new data by the radar and transmission of previously stored data to the ground. The high accuracy position control of the satellite is implemented by means of star sensors that are installed near the radar antenna, so that the required high accuracy of the antenna alignment of

Operational life	5+5 years (DLR expectation: beyond 2018)
Launch date	15 June 2007, 4:14 CEST
Launch site	Baikonur, Kazakhstan
Antenna size	4.788 m x 0.7 m
Launch mass	1230 kg
Payload mass	~400 kg
Radar frequency	9.65 GHz (X band)
Power consumption	800 W (on average)
Repeat Period	2.5-11 days (depending on the imaging mode)
Orbital altitude	514 km
Inclination	97.44°
Nominal acquisition direction	Right side
Polarisation	Single, dual (depending on imaging mode)

Table 2.2 – TerraSAR-X technical data

65 arcsecs can be achieved. A Global Positioning System (GPS) receiver located on board enables a precise determination of the orbit. The primary payload is a Synthetic Aperture Radar with an active antenna that allows for the utilization of different imaging modes and can be used in a very flexible manner. With radar instruments various frequency ranges of the radar spectrum can be observed, the so-called bands. TerraSAR-X is operated in the X-band, which is lying at a frequency around 9.65 GHz, corresponding to a wavelength of about 3 centimetres. The technology of the active, phase-controlled antenna enables a high flexibility and mission efficiency. While in case of passive systems the whole radar antenna or even the satellite must be rotated in order to align the antenna onto the target area, the active antenna of TerraSAR-X can steer its radar pulses in a certain direction. The antenna is 4.80 meters long and 80 centimetres wide. The satellite is designed in a way that it can be installed, together with its antenna at its full size, on the launch vehicle. In this way a complex unfolding mechanism can be avoided.

Alongside the SAR instrument two secondary payloads are flying on TerraSAR-X:

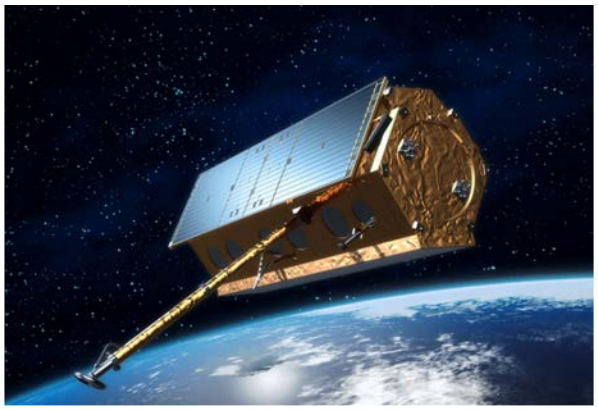

Fig. 2.13 – TerraSAR-X satellite

1. The *Laser Communication Terminal (LCT)*: a technology demonstrator that is used for in-orbit verification of rapid optical data transfer in space. Moreover, data could be successfully transmitted to a ground station. Later on, it will be possible to transmit large quantities of data operationally to the ground by means of this new type of laser system. This technology basically enables an extremely rapid data exchange via relay stations around the world.

2. The *Tracking, Occultation and Ranging Experiment (TOR)*: consists of the IGOR dual frequency GPS receiver together with a laser reflector unit. IGOR allows a highly accurate determination of the satellite orbit with an accuracy of up to just a few centimetres, which enhances the quality of the radar images. IGOR is also used to conduct radio occultation measurements in the atmosphere and the ionosphere. Here IGOR records the signals of the GPS satellites that are appearing or disappearing on the Earth's horizon.

Evaluation of these measurements allows conclusions to be drawn concerning pressure, temperature, water vapour content, and electron density in the atmosphere, which can be used, for example, in the improvement of numerical weather models, or investigations into climate

change. With the laser reflector unit it is possible by means of a laser measuring network installed on the Earth to measure the exact distance of the satellite to the individual receiving stations, which similarly supports an exact determination of the orbit.

Chapter 3

3-D SAR imaging

Due to the specific SAR geometry, SAR imaging represents a projection of the 3D space (x, y, z) into the bi-dimensional (2D) cylindrical zero-Doppler coordinates (x, r). For each pixel of a SAR image, the scattering response consists of a sum of contributions from all scatterers at the same range, encompassing all heights. Hence information about the vertical structure is lost. To recover such information, 3-D imaging techniques are required, whose derived secondary products consists in Digital Elevation Model (DEM), i.e. data files that contain information on the spatial distribution of the elevation data over a specified area. In particular, one may distinguish between DSM, representation of the first reflective or visible surface (including trees, buildings, and any other features which is elevated above the ground), and Digital Terrain Model (DTM), representation of the bare terrain (without objects).
In the following sections we present the basis of three 3-D imaging techniques: (i)Radargrammetric SAR (StereoSAR) [46] and (ii)Interferometric SAR (InSAR) [29], both based on the use of two complex-valued radar images acquired from, respectively, different and slightly different point of view, and (iii)Tomographic SAR (TomoSAR) [56], evolution of (ii) and based on the use of more than two SAR acquisitions performed in interferometric configuration.

3.1 Radargrammetric SAR

Radargrammetry was first employed in the 1950s with ground and airborne radar, then less and less, due to the quite low amplitude resolution of radar satellite imagery and, consequently, the high loss in term of accuracy [41]. Only within the last decade, thanks to the very high resolution imagery acquired by new satellite sensors, as COSMOSkyMed (Italian), TerraSAR-X (German) and RADARSAT-2 (Canadian), which are able to supply imagery with 1 m GSD, the radargrammetric approach has been revitalized and investigations restarted [11, 48, 50, 63]. A comprehensive text on radargrammetry is [41].

Analogous to optical photogrammetry, radargrammetry is based (at least) on a stereopair that must be acquired under a suited geometric configuration. This technique exploits only the amplitude information from SAR imagery and coherence between images is not required. Respect to InSAR, the independence from the coherence is one of the main advantages of StereoSAR, especially from the point of view of the strong influence of the land cover and the atmospheric effects. Basically, atmospheric effects on the SAR imagery are same in the StereoSAR or in the InSAR processing. However, as mentioned, StereoSAR uses the magnitude (intensity) value whereas InSAR uses the phase difference in SAR imagery. Considerably, magnitude is less affected than phase by atmospheric heterogeneity. Hence, the atmospheric disturbance is undesirable for the interferometric processing but not much of a concern for the radargrammetric one.

The radargrammetric approach performs a 3-D reconstruction based on the determination of the sensor-object stereo model for which the position of each point on the object is computed as the intersection of two radar rays coming from different positions and, therefore, with two different look angles (Fig. 3.1). Radargrammetry is based on stereogrammetry, which is a classical method for relief reconstruction using optical

remote sensing images. Stereo viewing reproduces the natural process of stereovision. As for photogrammetry, two steps are required for DSM generation: stereopair orientation and image matching for point cloud generation. In [12] a complete procedure for generating radargrammetric DSMs is proposed.

In the context of the orientation models for the stereo pair, two main

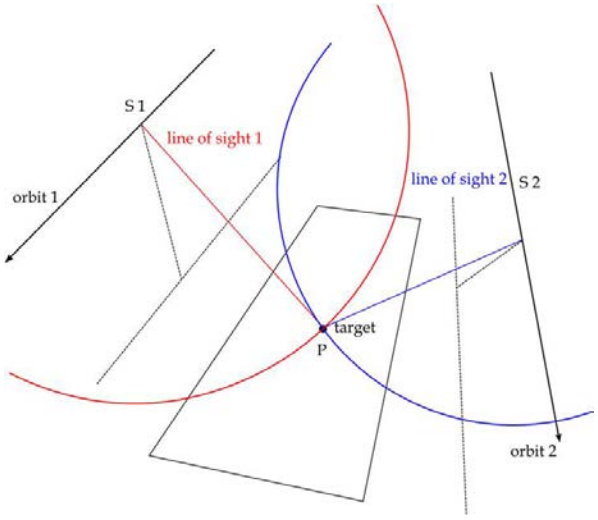

Fig. 3.1 – StereoSAR acquisition system in zero Doppler geometry

kinds of models are adopted: the physical sensor models (also called rigorous models) and the generalized sensor models. In the first one, in case of SAR imagery, the image and the ground coordinates are linked through the radargrammetric equations (similarly to collinearity equations in photogrammetric approach) and the involved parameters have a physical meaning. Besides, they require knowledge on the specific satellite and orbit characteristics. On the contrary, the generalized models are usually based on the Rational Polynomial Functions (RPFs), which link image and terrain coordinates by the Rational Polynomial Coefficients (RPCs) and do not need the knowledge about the sensor and acquisition features. The RPCs can be calculated by the final users via a Least-Squares (LS)

estimation directly from Ground Control Points (GCPs), or proprietarily generated by the sensor managing companies based on their own physical sensor models and distributed to users through imagery metadata. Nevertheless, the first strategy (also called terrain-dependent) is not recommended if a reliable and accurate orientation is required. In the second strategy, they can be generated according to a terrain-independent scenario, using known physical sensor.
In [13], following from [41], is proposed a model based on two fundamental equations: the first equation of (3.1) represents the general case of zero-Doppler projection: in zero-Doppler geometry the target is acquired on a heading that is perpendicular to the flying direction of satellite; the second equation of (3.1) is the slant range constrain.

$$\begin{cases} V_{XS} \cdot (X_S - X_P) + V_{YS} \cdot (Y_S - Y_P) + V_{ZS} \cdot (Z_S - Z_P) = 0 \\ \sqrt{(X_S - X_P)^2 + (Y_S - Y_P)^2 + (Z_S - Z_P)^2} - (D_S + CS \cdot I) = 0 \end{cases} \tag{3.1}$$

X_P, Y_P, Z_P are the coordinates of the generic Ground Point (GP) in a terrestrial coordinate system (time independent); X_S, Y_S, Z_S are the coordinates of the satellite sensor in the same coordinate system (time dependent); V_{XS}, V_{YS}, V_{ZS} are the cartesian components of the satellite sensor velocity again in the same coordinate system (time dependent); D_S is the so-called near range, a parameter related to the range measurements whose initial value is available in the metadata; CS is the slant range resolution or column spacing; I is the column position of point P on the image. The orbital arc related to an image acquisition in Spot-Light mode, since quite short (about 10 km), is conveniently interpolated with Lagrange polynomial using the orbital state vectors available in the metadata. In this way, it is possible to model the images acquisition and the stereo orientation through metadata parameters.

The image matching process heavily impacts the DSM accuracy, and its efficiency depends on the configuration for the radargrammetric appli-

cation. Observing the target in opposite-site view allows to obtain a good stereo geometry, but causes large geometric and radiometric disparities that hinder image matching. Thus, in order to increase the efficiency, a good compromise is to use a same-side configuration stereo-pair with a base to height ratio ranging from 0.25 to 2 [46]; ; anyway, it is better to limit within 0.35 and 0.70. Two are the main steps of image matching process: the definition of a matching entity, that is a primitive in the master image to be compared with a portion of other slave images, in order to identify correspondences among them; the selection of a search criteria in order to limit the possible solutions and to avoid mismatching.

In [49] an original matching procedure is proposed. The matching strategy is based on a coarse-to-fine hierarchical solution with an effective combination of geometrical constrains and an Area Based Matching (ABM) algorithm, using a pyramidal approach and analysing the SNR. In this way the surface model is successively refined step by step, until the last step (corresponding to the original image resolution) where the final dense and accurarate DSM is reconstructed (see Fig. 3.2).

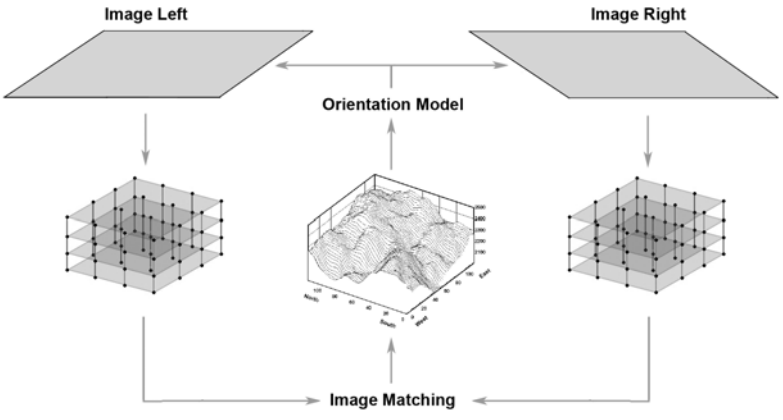

Fig. 3.2 – Geometrical constrain and voxel generation

3.2 Interferometric SAR

In the last two decades InSAR has been developed from theoretical concept to a technique that is being utilized at an increasing rate for a wide range of Earth science fields. Despite the fact that none of the currently deployed imaging radar satellite platforms was designed with interferometric applications, the high quality and large quantity of exciting results from this technique have demonstrated their potential as powerful tools for ground deformation evaluation [45, 69] and DEM generation [17, 26]. In the last few years InSAR capability has been considerably improved by using large stacks of SAR images acquired over the same area, instead of the classical two images used in the standard configurations [18, 40]. Special missions, such as the Shuttle Radar Topography Mission (SRTM) [4, 54], or more recently TanDEM-X (ongoing) [37], have been designed and built to yield elevation data on a world scale. At least a pair of images of the same area acquired from slightly different look angles are needed to perform the 3-D reconstruction. Such can be obtained either simultaneously using two radar antennas mounted on the same platform (single pass interferometry) or at different times by exploiting repeated orbits of the same satellite (repeat pass interferometry).
Fig. 3.3 shows the interferometric acquisition geometry and relative notations related to two radar measurements of the same point (P) observed from slightly different looking angles (θ_1,θ_2). The distance between the two satellites S_1,S_2 in the plane perpendicular to the orbit is called the interferometer baseline B. Respect to its inclination angle α_B in the incidence plane, B can be decomposed into its perpendicular $B_\perp$ and parallel $B_\parallel$ components:

$$B_\perp = Bcos(\theta_1 - \alpha_B) \quad \text{and} \quad B_\parallel = Bsin(\theta_1 - \alpha_B) \tag{3.2}$$

The two SAR images are composed of a regular grid with complex values, s_1 and s_2, which can be decomposed in an amplitude and phase

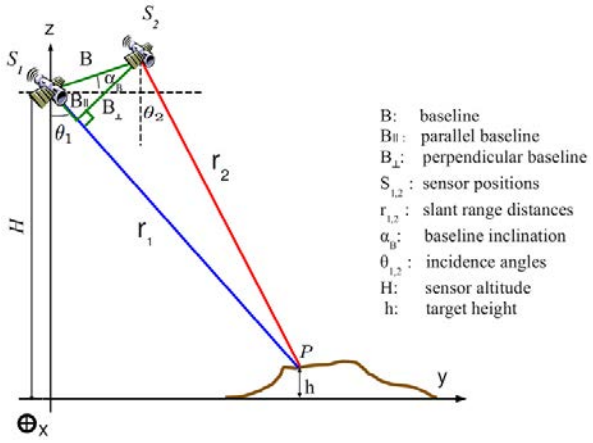

Fig. 3.3 – Geometry of interferometric SAR system

component using:

$$s_1 = |s_1|e^{-j(\phi_{r1}+\phi_{obj1})} \qquad s_2 = |s_2|e^{-j(\phi_{r2}+\phi_{obj2})} \tag{3.3}$$

where $\phi_{ri} = kr_i$, with $i = 1, 2$ and $k = 4 \cdot \pi\lambda$, where λ is the wavelength. Before the interferometric processing, the image pair must be at first coregistered, i.e. the slave (s_2) grid will be aligned and resampled to corresponding locations in the master (s_1) grid. After that, the SAR interferogram is generated by cross-multiplying, pixel by pixel, the first SAR image with the complex conjugate of the second[16]. Assuming that the proper scattering phase of the scatterer is the same in both SAR images due to the similar look angles (as true as the smaller the signal decorrelation), i.e. $\phi_{obj1} = \phi_{obj2}$, one can obtain

$$s_1 s_2^* = |s_1||s_2|e^{-jk(r_1-r_2)} = |s_1||s_2|e^{-jk\Delta r} \tag{3.4}$$

Thus, the interferogram amplitude is the amplitude of the first image multiplied by that of the second one, whereas its phase (the interfero-

metric phase) is the phase difference between the images

$$\phi_{inf} = \arg\{s_1 s_2^*\} = -k\Delta r + 2\pi n \text{ with } n = 0, \pm 1, \pm 2, ... \tag{3.5}$$

which is 2π ambiguous, i.e. $\phi_{inf} \in [-\pi, \pi]$. The phase differences of radar wavelengths recorded by SAR images are able to provide precise measurement, to the sub-wavelength level, of the range or distance between the location of the observing antennas and the points of reference (pixel centres). With two observing antennas, or the same antennas at different satellites overpass times, differential phases can provide information on terrain elevation or on terrain displacement [65].
The plane wave approximation in the far-field (i.e. parallel ray approximation), can be applied to the interferometric acquisition geometry in Fig. 3.3 and we obtain

$$B_{\parallel} = Bsin(\theta_1 - \alpha_B) = \Delta r - \frac{\Delta r^2}{2r_1} + \frac{B^2}{2r_1} \simeq \Delta r \tag{3.6}$$

since the baseline B and the range difference Δr are largely inferior to the distance between the master track and the scatter, r_1. The interferometric phase is then proportional to the parallel part of the baseline.

SAR images have a spatial resolution defined by the pulse length, altitude of the satellite and look-angle. The slant range resolution is half the pulse length. The ground range resolution is defined as the slant range resolution divided by the sine of the look-angle. The set of phase differences ϕ_{inf} produced for all pixels of the two SAR images is used to generate an interferogram. We can linearise this variation into two contributions respectively related to the slant range displacement, Δr_1 and the height variation, Δz,

$$\phi_{inf} = \frac{\partial \phi_{inf}}{\partial r_1}\Big|_{h_r} \Delta r_1 + \frac{\partial \phi_{inf}}{\partial z}\Big|_{r_1} \Delta z = \Delta\phi_{fe} + \Delta\phi_{topo} \tag{3.7}$$

The resulting two components correspond to the *flat earth phase* and the

topographic phase respectively.

The flat-earth effect is related to the ellipsoid reference and consists of numerous fringes parallel to the flight path (see Fig. 3.5a). A shown in Fig. 3.4a, slightly moving along the ground direction y with constant height h_r, the interferometric phase variation due to the slant range variation Δr_1, can be written as:

$$\Delta\phi_{fe} = \frac{kB_\perp \Delta r_1}{r_1 tan\theta_1} \tag{3.8}$$

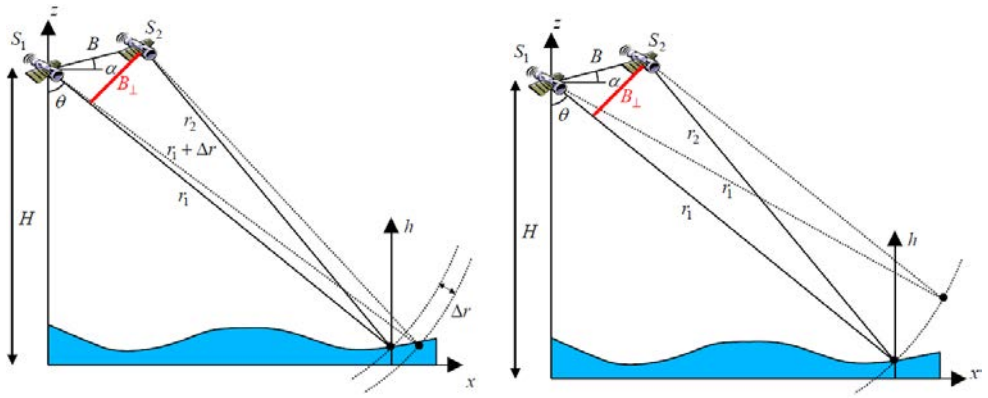

(a) Flat earth (b) Topography

Fig. 3.4 – Interferometric phase variations with range r and height z, related respectively to the flat earth effect and the topography

The topographic phase is directly linked to the surface height information. As shown in Fig. 3.4b, slightly increasing the height of the scatterer by Δz, while maintaining the sensor-scatterer distance at r_1, the interferometric phase due to the height variation Δz, can be expressed as

$$\Delta\phi_{topo} = \frac{kB_\perp \Delta z}{r_1 sin\theta_1} \tag{3.9}$$

The height sensitivity can be respresented by the *vertical wavenumber* k_z

and the *height ambiguity* is defined by h_{amb} when $\Delta\phi_{topo} = 2\pi$

$$k_z = \frac{kB_\perp}{r_1 sin\theta_1} \tag{3.10}$$

$$h_{amb} = \frac{2\pi}{k_z} = \frac{\lambda}{2}\frac{r_1 sin\theta_1}{B_\perp} \tag{3.11}$$

When the scatterer is located at $h_r > h_{amb}$, e.g. mountains or skyscrapers, the measured topographic phase is wrapped and can be represented as

$$\Delta\phi_{topo} = \lfloor k_z h_r \rfloor_{2\pi} \tag{3.12}$$

with $\lfloor\rfloor_{2\pi}$ expressing 'modulo 2π'. To calculate the real height of the scatterer, a reference point P_{ref} should be firstly selected with known height h_{ref}. In the neighbourhood of P_{ref}, we compute the h_r from $\Delta\phi_{topo}$ by equation (3.9).

The interferometric coherence γ is defined by [8] as a normalized complex cross-correlation between two received signals s_1 and s_2

$$\gamma_{int} = \frac{E\{s_1 s_2^*\}}{\sqrt{E\{|s_1^2|\}E\{|s_2^2|\}}} \tag{3.13}$$

Its phase is the expected interferometric phase ϕ_0 of the selected pixel and its magnitude is related to phase noise. Thus, the coherence measures the interferogram quality and influences the estimation of interferometric phase, since it is related to phase stability or predictability. Receiver noise, for example, may render the two images to be not fully correlated, i.e. $|\gamma| < 1$. It is known from [8] that the variance of estimation errors of ϕ_{inf} increases when γ_{int} descreases. In Fig. 3.5c it is depicted the coherence image generated over a cropped area of the Berlin city: brighter areas (good coherence) correspond mainly to man-made targets, while darker areas (bad coherence) mainly to vegetated zones.

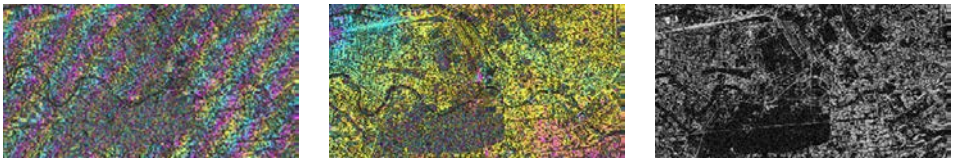

(a) ϕ_{inf} (b) ϕ_{topo} (c) $|\gamma|$

Fig. 3.5 – Interferometric phase, topographic phase and interferometric coherence (Berlin urban area)

3.3 Tomographic SAR

Currently, tomographic SAR (deeply investigated in chapter 4) represents the most effective SAR technology for the monitoring of complex areas, such as, for example, urban scenarios. It is an evolution of the interferometric approach by extending one scattering phase center [8] to several scatterers by using a coherent combination of images acquired in multi-baseline interferometric configuration and performing a 3-D imaging by the formation of an additional synthetic aperture in elevation [56]. This technique directly retrieves the distribution of the backscattered power in the vertical direction, as shown in Fig. 3.6.

TomoSAR allows also to solve the geometric distortion problems, which are intrinsic with the SAR system, in areas characterized by a high density of vertical structures, such as dense urban areas, where it happens that radar returns signal responses belonging to different parts of the single structure under observation that interfere in the same SAR resolution cell. This technique, being able to analyze the distribution at the different heights of the backscattering energy, is able to solve this interference and separate different targets inside the same pixel (i.e. to solve the layover effect). Furthermore, by analysing dataset of images distributed in time, is even possible to estimate the deformation affecting each single interfering target, through the extraction of its deformation time series.

TomoSAR is also a valuable technique to achieve detailed and veritable DSM of the observed scene, allowing the possibility to extract detailed

and spatial dense 3-D models of the whole observed scene or of the single structures on ground (such as buildings). For this reason, tomographic reconstructions have started to be considered competitive with results obtained through an analysis based on the usage of optical sensors, such as LiDAR, which are typically exploited for the 3-D reconstructions of buildings. With respect to the latter, SAR tomography offers the further advantages of a temporal monitoring as well as synoptical view.

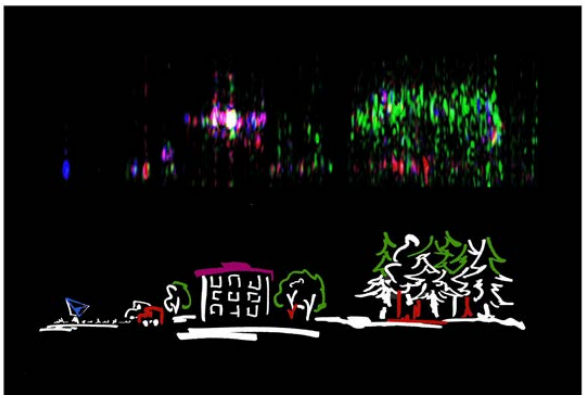

Fig. 3.6 – SAR tomographic representation [56]

Chapter 4

SAR Tomography

Tomographic SAR focusing is a 3-D imaging technique based on the formation of an additional synthetic aperture in the elevation direction in order to achieve a substantially improved resolution. As extension of the interferometric SAR, it consists in a coherent combination of a set of images (stack) acquired from several orbit (satellite systems) or flight (airborne systems) tracks in a MB-InSAR configuration that allows a direct localization and separation of multiple scattering contributions within a range-azimuth resolution cell. TomoSAR is also a valuable technique to achieve detailed and veritable DSM of the observed scene, allowing the possibility to extract detailed 3D models of single structures on ground (such as buildings) and to monitor them in terms of temporal deformation (four-dimensional (4D)) at high resolution. These two aspects represent an important development in SAR remote sensing especially for the analysis of dense urban scenarios. Thanks to the first one, this technology allows to resolve the signal scatterings superposition due to the layover that frequently affects these areas as scenes rich of man-made structures. The second aspect represents an important advantage in the urban and environmental monitoring and in the management of risk situations.
In the following sections an overview of this technique is given, including a short survey about the state-of-the-art, the basic principles and the

spectral estimation techniques used for the present study.

4.1 State-of-the-art in urban areas

The word tomography is derived from two ancient Greek words: *tomos*, i.e. 'slice, section', and grapho, i.e. 'to write'. Therefore, this technique allows to generate detailed images of a specific plane section of a solid object by using changing information coming from any kind of penetrating wave. In this sense, the tomography represents a valuable tool for several scientific applications as the geophysical, the archaelogical or the medical ones. In the SAR remote sensing field, the highly investigation of the tomography is due to the desire to achieve a fully 3-D imaging starting from a 2-D SAR image. Moreover a 4-D SAR tomographic imaging allows to describe the space-time or space-velocity information and then to monitor the target deformation.
First important experiments have concerned the analysis of volume structures, such as forests, using low frequencies (e.g. L- or P-band) airborne sensors. The first application is represented by [56], where the concept of the formation of a second synthetic aperture in the direction of the translational movement is presented. The experimental results have been achieved using MultiBaseline (MB) L-band data sets acquired by the DLR's E-SAR (airborne) system. A method for reduction of the height ambiguities associated to the irregular and undersampled spatial distribution of the imaging positions is proposed and, as mentioned by the authors, this work represents the first step into SAR tomographic technique that showed its great potential in respect to several applications. Accordingly, over the years different papers have been published about the tomographic SAR techniques application in order to retrieve the forest structures [60, 33, 62], to estimate ice thickness [61] or building heights [70, 23, 32], to solve the layover problem induced by strong terrain slopes or discontinuities in the imaged scene, especially in complex urban ar-

eas [9, 34, 55, 53]. An overview is given in [19] and the potentialities of TomoSAR combined with polarimetric diversity are demonstrated for a wide variety of applications, such as forests remote sensing, detection of under-foliage object and urban areas characterization.

Built-up area analysis has been always a great challenge in particular starting from the availability of the first sensors able to provide sufficient resolution. Speaking about space-borne platforms, in the last decade the new satellite generation, well represented by the German TerraSAR-X (TSX) and the Italian COSMO-SkyMed (CSM) ones, provided high resolution data both in terms of space and time. Complex urban scenes, being rich of man-made structures, are considered as complex scenarios needed of a refined analysis as the observations are frequently affected by layover effects. In fact, a mixture of diverse scattering patterns (such as double bounce reflection due to wall-ground reflections, single bounce from roofs and from the ground, volumetric scattering due to potential vegetation) may interfere in the same SAR resolution cell (see subsection 2.2.1). In literature, the tomographic study of dense urban environment characterization has been mainly performed from two different point of view: using full polarimetric MB data acquired by airborne sensors (e.g. E-SAR) or using Single Polarization (SP) MB data acquired by satellite sensor (e.g. TerraSAR-X).

Regarding the former, in [20], [32] and [57] several demonstrations of the effectiveness of different spectral estimation methods for building height estimation and scatterers physical properties retrieval are given using fully polarimetric MB-InSAR data over the city of Dresden acquired by the E-SAR system.

Regarding the latter, in literature different studies about the 3-D and the 4-D tomography and the layover correction have been published. In particular passing through [70-74] one may appreciate the description of several decomposition methods and the relative comparisons presented by the authors. The papers concern the detection of multiple targets

within the same azimuth-range cell and a 3-D mapping of the scattering properties of the illuminated scene [71], the extension of the tomographic concept to the 4-D differential case [72] and to the Compressive Sensing (CS) [1] technique [70-72] applied to the tomographic imaging of the deformations of urban infrastructures. The works represent an important demonstration of the tomographic potentialities of the high resolution TSX sensor, using data acquired over the city of Las Vegas. On the other side, several investigations about the tomographic capability to resolve layover cases, e.g. separating single and double-scattering mechanisms within imaged pixels, are performed in [21-24, 55] .The results have been achieved processing datasets acquired at first from ERS-1 and ERS-2 and then from TSX and CSM satellites over different cities (such as Naples and Rome). The works aim to describe several algorithms for the reconstruction and monitoring of the whole 3-D structure of buildings, exploiting both the 4-D imaging [22, 55] and the combination of TomoSAR techniques and CAESAR, a method proposed in [21, 24] that allows the identification of multiple scattering mechanisms from the analysis of the covariance matrix.

In this context it is collocated the present research aimed to perform a global three-dimensional characterization of dense and complex urban areas by means of the classical spectral estimators. In particular, the possibility to correct the geometric distortions due to the layover and to determine the information about the number of scatterers (up to three) and the corresponding reflectivity within one resolution cell have been evaluated. Several 3-D reconstructions of single structures have been performed both in term of buildings heights and vertical reflectivity. Moreover an innovative time stability analysis of the observed scene have been carried out in order to detect the stable and unstable scatterers.

[1] The Compressive Sensive [10] is a signal processing technique for the reconstruction of super-resolved signals and images starting from far fewer data/measurements than what is usually considered necessary. As a favorable sparse reconstruction technique, it represents a valuable method to perform 4-D SAR tomography.

The processing have been performed using an adequate high resolution MB-InSAR data acquired over Paris urban area by the satellite TSX. The final goal is to demonstrate the high potentialities of tomographic techniques using basic mono-dimensional estimators as Beamforming, Capon and MUSIC combined to very high resolution data.

4.2 Basic principles

The objective of tomographic focusing is to estimate the height profile of a medium and the corresponding set of reflectivity coefficients ($\sigma(z)$). The basic principle of satellite TomoSAR focusing is illustrated in Fig. 4.1. In order to achieve focusing in height direction and to generate a 3-D SAR image, the additional aperture is synthesized in the normal direction $\hat{n}$, perpendicular to the range (line-of-sight) $\hat{r}$ and the azimuth $\hat{x}$ directions. This normal direction can be projected onto the elevation direction $\hat{z}$ or the ground range direction $\hat{y}$ in case of, respectively, airborne or satellite systems. The former consider parallel flight tracks at different elevations; while the latter consider different, as equally spaced as possible, orbit tracks at the same elevation (Fig. 4.1). Following formulations are referred to airborne geometry.

A scatterer can be assumed as a source that emits a signal s towards the SAR. In order to characterize a scatterer (or a source), L samples (or looks or realizations) of its response are acquired and processed. The corresponding signals can be characterized from the statistical properties relating the L realizations of their response, i.e. $s(l)_{l=1}^{L}$.
For a scatterer located at the height n_0 and at a range position $r(z, n_0)$, the received signal can be expressed as:

$$s(z, n_0) = a(r_0, n_0) * exp\{-jkr(z, n_0)\} \tag{4.1}$$

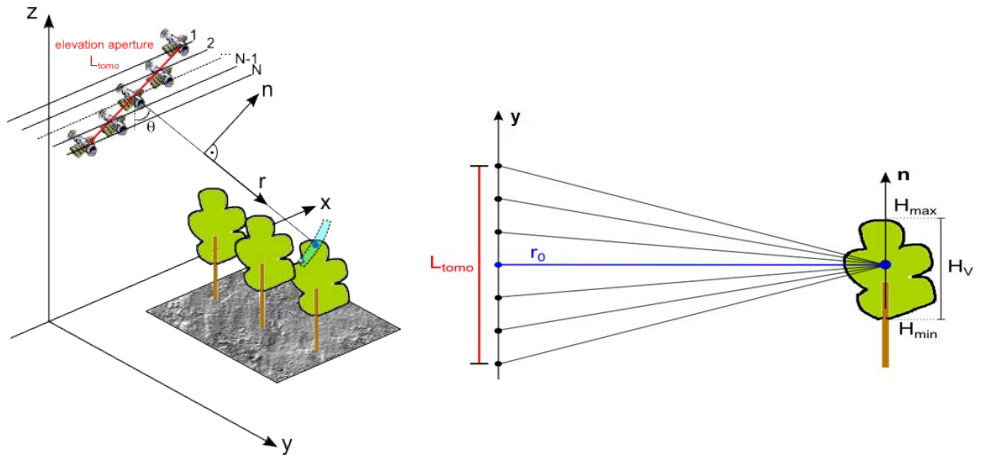

(a) TomoSAR geometry

(b) After deramping (flat earth compensation) geometry

Fig. 4.1 – Tomographic SAR satellite imaging geometry

with $r(z,n_0) = \sqrt{r_0^2 + (z-n_0)^2} \simeq r_0 + \frac{(z-n_0)^2}{2r_0}$. In equation (4.1) r_0 is the minimum range distance between the sensor and the scatter, and $a(r_0,n_0)$ is the complex reflectivity of the scatterer at the position (r_0,n_0) for a given azimuth position x_0 and $'*'$ indicates the convolution between the scattering response and the impulse response of the TomoSAR system. After the demodulation, the received signal becomes:

$$s_d(z,n_0) = a(r_0,n_0) * exp\left\{-jk\frac{(z-n_0)^2}{2r_0}\right\} \tag{4.2}$$

which includes the quadratic phase term as a chirp signal in the $\hat{z}$ direction. Thus, the vertical spatial frequency (or vertical wavenumber) k_z is given by:

$$k_z(z,n_0) = \frac{\partial arg(s_d(z,n_0))}{\partial z} = \frac{k}{r_0}(n_0 - z) \tag{4.3}$$

and is a function of the elevation z. After *deramping* which consist in multiplying the received signal with a deramping function

$$u(z) = exp\left\{jk\frac{z^2}{2r_0}\right\} \tag{4.4}$$

and the deramped signal can be obtained as follows

$$s_{dr}(z, n_0) = a(r_0, n_0) * exp\left\{-jk\frac{(n_0^2 - 2zn_0)}{2r_0}\right\} \tag{4.5}$$

The vertical wavenumber k_z of the deramped signal s_{dr} is hece given by

$$k_z(n_0) = \frac{\partial arg(s_{dr}(z, n_0))}{\partial z} = \frac{kn_0}{r_0} \tag{4.6}$$

which is independent of the z position but only depends on the scattering height n_0 inside a volume with a total height equal to H_V (see Fig. 4.1b). Then, applying FFT to the deramped signal $s_{dr}(z, n_0)$ in the $\hat{z}$ direction, the focused image for this scatterer may be represented by $S_{dm}(k_z, n_0)$

$$S_{dm}(k_z, n_0) = a(r_0, n_0)L_{tomo}exp\left\{-jk\frac{n_0^2}{2r_0}\right\} sinc\left(\frac{kL_{tomo}}{2r_0}(n_0 - n)\right) \tag{4.7}$$

The tomographic resolution depends on the width of this sinc-function and is given by

$$\delta_z = \frac{\lambda r_0}{2L_{tomo}} \tag{4.8}$$

where r_0 is the slant range distance of the master acquisition, located in the center of the tomographic constellation. L_{tomo} is the tomographic illumination distance and equivalent to the largest baseline length in case of an MB-InSAR configuration. Thus, a better geometric tomographic resolution requires a larger tomographic aperture L_{tomo}. In order to avoid height ambiguities, L_{tomo} should be properly sampled and fulfil the Nyquist criterion for the vertical bandwidth. The vertical bandwidth B_{sd} can be described by the variation of the vertical wavenumber (4.6) with respect to the observed volume, as follows:

$$B_{sd} = k_z(n_0) \tag{4.9}$$

with $n_0 \in [H_{min}, H_{max}], H_V = H_{max} - H_{min} = \frac{kH_V}{r_0}$. Therefore, the sampling distance d_s of L_{tomo} should verify the inequality

$$d_s \leq \frac{2\pi}{B_{sd}} = \frac{\lambda r_0}{2H_V} \tag{4.10}$$

which depends on the total height of the examined volume H_V. Assuming the tracks are evenly distributed with the baseline distance d_s, the tomographic resolution δ_z is directly related to the number of acquisitions N with $\delta_z \propto \frac{1}{N}$ and $N = \frac{L_{tomo}}{d_s} + 1$. This fact limits the geometric tomographic resolution since numerous acquisions require a high experimental effort. Another problem is that in practice tracks are unevenly distributed, implying ambiguities in height. These limitations may be fixed applying spectral analysis techniques that permit to obtain a high tomographic resolution with a moderate number of acquisitions and for a nonuniform baseline distribution.

4.3 Focusing techniques

The tomographic inversion is essentially a spectral analysis problem solved applying methods ranging from classical Fourier-based to high resolution approaches. In order to perform a refined analysis of volumetric structures of the observed scenes, these techniques are applied to MB-InSAR data sets in order to localize multiple scattering contributions within a range-azimuth resolution cell and their height z_i. The joint processing of fully polarimetric data sets acquired in a Polarimetric MB-InSAR (MB-PolInSAR) configuration, using Polarimetric SAR Tomography (PolTomSAR), permits to analyse scattering mechanisms within volumetric structures and extract some physical features [19].

After an introduction about the MB-InSAR signal model, this section introduces nonparametric and parametric spectral analysis techniques

used in the present work in order to estimate the height and the reflectivity of the detected scatterers. Generally, nonparametric spectral analysis techniques are considered as robust, since they do not require any assumptions about the statistical characteristics of the received signals, but possess a limited resolution. In cases where an appropriate data model exists, model-based or parametric approaches yield generally superior estimation accuracy but require to determine the number of sources D located in each pixel under study.

4.3.1 MB-InSAR signal model

A SAR image resolution cell is the results of the combination of all the complex signal scattering contributions derived by real environments whose radial distances fall within the domain affected by the SAR impulse response, but with different elevation angles θ. Therefore, in practice, the total source signal can be modelled as a sum of D scattering contributions within a range-azimuth resolution cell

$$s(l) = \sum_{d=1}^{D} s_d(l) \tag{4.11}$$

On the basis of the nature of the observed scattering, the backscattered signal can be modelled in two different ways: as deterministic and as distributed. The former regards signals affected by speckle noise and the huge number of scatters contained within one resolution cell cannot be separated; the latter is related to a dominant and stable scatterer lying within the selected resolution cell. Assuming that D scatterers are located in the same resolution cell and partially correlated, the received signal may be considered as a mixture of distributed and deterministic scattering responses, called hybrid scatterers.
In Fig. 4.2 the MB-InSAR acquisition geometry is represented. It consists of M SAR acquisitions, each pair of which are separated by a base-

line. The baseline distance between the master position and the jth

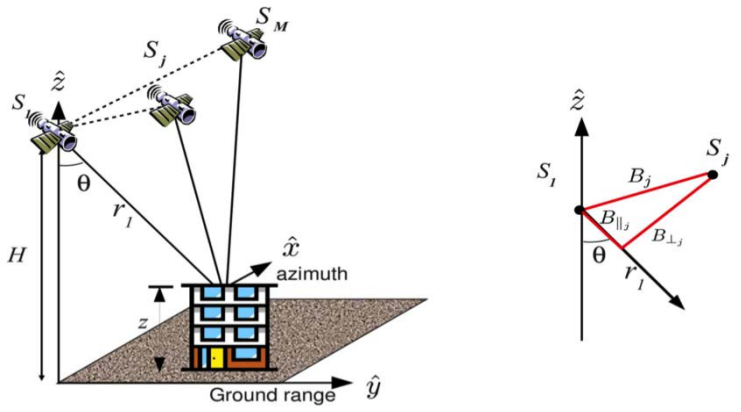

Fig. 4.2 – MBInSAR geometrical configuration

position, noted B_j, can be decomposed into $B_{\parallel j}$, a component parallel to the slant range direction, and a perpendicular one, $B_{\perp j}$, aligned with the cross-range direction. Considering an azimuth-range resolution cell that contains D backscattering contributions from scatterers located at different heights and assuming no decorrelation between the different acquisitions, the data vector measured by M, $\mathbf{y} \in \mathbb{C}^{Mx1}$, can be formulated as follows:

$$\mathbf{y}(l) = \sum_{d=1}^{D} s_d \mathbf{a}(z_d) + \mathbf{n}(l) = \mathbf{A}(\mathbf{z})\mathbf{s} + \mathbf{n}(l) \tag{4.12}$$

where $l = 1, ..., L$ indicates one of the L independent realizations of the signal acquisition, also called looks. The source signal vector, $s = [s_1, ..., s_D]^T$, contains the unknown complex reflection coefficient of the D scatterers, and $\mathbf{n} \in \mathbb{C}^{Mx1}$ represents the complex additive noise, assumed to be Gaussianly distributed with zero mean and variance σ_n^2, and to be white in time and space. The steering vector $a(z)$ contains the interferometric phase information associated with a source located at the elevation position z above the reference focusing plane and is given by:

$$\mathbf{a}(z) = [1, exp(jk_{z_2}z), ..., exp(jk_{z_M}z)]^T \tag{4.13}$$

where $k_{z_j} = \frac{4\pi}{\lambda}\frac{B_{\perp_j}}{r_1 sin\theta}$ is the two-way vertical wavenumber between the master and the jth acquisition tracks. The carrier wavelength is represented by λ, whereas θ stands for the incidence angle and r_1 is the slant range distance between the master track and the scatterer. The steering matrix $\mathbf{A(z)}$ consists of D steering vectors corresponding each to a backscattering source:

$$\mathbf{A(z)} = [\mathbf{a}(z_1), ..., \mathbf{a}(z_D)] \tag{4.14}$$

with $z = [z_1, ..., z_D]^T$, the vector of unknown source heights. The data covariance matrix $\mathbf{R}$ can be represented as:

$$\mathbf{R} = \mathbf{A}\mathbf{R_s}\mathbf{A}^\dagger + \mathbf{R_n} \tag{4.15}$$

where $\mathbf{R_s} = E(\mathbf{s}\mathbf{s}^\dagger)$ is the source covariance matrix describing the correlations between the responses of the D scatterers and $\mathbf{R_n} = E(\mathbf{n}\mathbf{n}^\dagger) = \sigma_n^2\mathbf{I}_{(MxM)}$ is the white noise covariance matrix.
Considering now interferometric decorrelation between different acquisitions, the initial model in equation (4.12) may be reformulated as a sum of contributions from random sources [27]:

$$\mathbf{y}(l) = \sum_{d=1}^{D} \mathbf{x}_d(l) \odot \mathbf{a}(z_d) + \mathbf{n}(l) = \sum_{d=1}^{D} \mathbf{y}_d(l) + \mathbf{n}(l) \tag{4.16}$$

where $\mathbf{x}_d \in \mathbb{C}^{Mx1}$ is unknown and accounts for both the reflection coefficient of the dth source, s_d, and its potential variations between the interferometric acquisitions over the L realizations. Depending on the type of scatterer under observation, the source signal $\mathbf{x}_d$ possesses varying statistical properties.
Considering the set of D backscattering contributions, the source covari-

ance matrix $\mathbf{R}_s$ is expressed as:

$$\mathbf{R_s} = \begin{bmatrix} \sigma_1 & \sigma_{12}\rho_{12} & \dots & \sigma_{1D}\rho_{1D} \\ \sigma_{12}\rho_{12}^* & \sigma_2 & \dots & \sigma_{2D}\rho_{2D} \\ & & \ddots & \\ \sigma_{1D}\rho_{1D}^* & \dots & \dots & \sigma_D \end{bmatrix} \tag{4.17}$$

with $\sigma_{dd'} = \sqrt{\sigma_d \sigma_d'}$ and $\rho_{dd'}$ the correlation coefficient between two sources. The covariance matrix described in equation (4.18) is generally considered as constant over the different acquisitions and can be computed as $\mathbf{R}_s(d, d') = E\{\mathbf{y}_{d_k}\mathbf{y}_{d'_k}^*\}$, $\forall k$, where $E()$ is the expectation operator.
The correlation of the dth source signal over the M acquisitions may be represented under the form of a normalized covariance matrix $\mathbf{R}_{\mathbf{x}_d}$ containing interferometric coherences, determined by the observed source and the geometrical configuration of the acquisitions:

$$\mathbf{R}_{\mathbf{x}_d} = \frac{1}{\sigma_d} E\{\mathbf{x}_d \mathbf{x}_d^\dagger\} = \begin{bmatrix} 1 & \gamma_{12} & \dots & \gamma_{1M} \\ \gamma_{12}^* & 1 & \dots & \gamma_{2M} \\ & & \ddots & \\ \gamma_{1M}^* & \dots & \dots & 1 \end{bmatrix} \tag{4.18}$$

4.3.2 Nonparametric tomographic estimators

Generally, nonparametric spectral analysis techniques are considered as robust, since they do not require any assumptions about the statistical properties of the received signals. Accordingly, they can be used in situations with lack of information about these properties. These methods aim to estimate the Directions Of Arrival (DOA), that is, given a spatially propagating signal, to determine its angle of arrival at the array. They respond to the following assumptions: (i) the signals with a given DOA θ are passed undistorted and (ii) all the other DOAs different from θ are attenuated as much as possible. These estimators rely entirely on the characterization of the Power Spectral Density (PSD) defined by the

periodogram or the correlogram, to provide the spectral estimates [59]. Their principal drawback lies in poor spectral resolution due to the high variance of the periodogram and correlogram estimates. In this section classical estimators like the Beamforming and the Capon method are presented for a MB-InSAR configuration.
For tomographic purpose, the goal is to determine an estimation $\hat{z}$ of the elevation of the scatterers under observation as the coordinates of the local maxima of an objective function with a scalar elevation argument $P(z)$:

$$\hat{\mathbf{z}} = \arg\max_{z,loc} P(z) \tag{4.19}$$

This objective function is given by the continuous estimate of the reflectivity, i.e. $P(z) = \hat{\sigma}(z)$.

4.3.2.1 Beamforming

The Beamforming method has been derived for estimating DOA as mentioned in [67, 35]. In [30], Beamforming was firstly suggested for solving the layover problem using MB-InSAR data sets. The Beamforming method for spatial frequency estimation can be derived as a Finite Impulse Response (FIR) filter [59], assuming a spatially white scenario, i.e. such a signal in the array output can be considered as impinging on the array with equal power from all direction θ. Minimizing the output power of the undesired interference, the filter is designed so as to maintain undistorted the signal at a given frequency, while attenuating signals at all other frequencies even though from many of them there might be no incoming signal.
The Beamforming spectrum is associated to the PSD of the received MB-InSAR data $\mathbf{y}(l)$, and its objective function is given by the continuous L-look estimate of the reflectivity:

$$P_B(z) = \hat{\sigma}_B(z) = \frac{1}{L}\sum_{l=1}^{L}\frac{|\mathbf{a}^{\dagger}(z)\mathbf{y}(l)|^2}{M^2} = \frac{\mathbf{a}^{\dagger}(z)\hat{\mathbf{R}}\mathbf{a}(z)}{M^2} \tag{4.20}$$

The beamforming DOA estimates are given by the locations of the n highest peaks of the function (4.20). Under the hypothesis of an uniform true reflectivity and for a sufficient number of looks L, the theoretical covariance $\mathbf{R}$ determined from the available finite sample $\{y(l)\}_{l=1}^{L}$ may be replaced by some estimate $\hat{\mathbf{R}}$ such as:

$$\hat{\mathbf{R}} = \frac{1}{L}\sum_{l=1}^{L}\mathbf{y}(l)\mathbf{y}^{\dagger}(l) \tag{4.21}$$

By means of equations (4.19) and (4.20) it is possible to estimate, respectively, the set of scatterer elevations $\hat{\mathbf{z}}$ and the corresponding reflectivities. Nevertheless, as shown in [59], if this method is consistent in the single-source case ($n = 1$), in the general case of multiple sources it leads to biased estimates for the height and reflectivity. This is mainly due to the poor resolution of the Beamforming estimator that limits the selection of discrete sources from peaks of the reflectivity spectrum. For the n single-source case, Beamforming can be shown to provide an approximation to the nonlinear LS DOA estimation method discussed in section 4.3.3.1 [59].
In order to get better resolution and reduce the leakage problems, the Capon method has been proposed.

4.3.2.2 Capon

The Capon method has been derived under the same condition of minimum interfering power as the Beamforming method, but considering the general case of nonwhite interference scenario. Contrarly to the Beamforming, the Capon filter is designed in a 'data-dependent' way aiming to steer to a certain DOA (or spatial frequency) θ and to attenuate any other signals that actually impinge on the array from a $DOA \neq \theta$. This method was applied for time series data in [14, 39], and array signal processing [59] as well as for MB-InSAR data processing [27].
In the MB-InSAR configuration, the Capon spectrum of the received

data is represented by the continuous estimate of the reflectivity:

$$P_C(z) = \hat{\sigma}_C(z) = \frac{1}{\mathbf{a}^{\dagger}(z)\hat{\mathbf{R}}^{-1}\mathbf{a}(z)} \tag{4.22}$$

The elevations of scatterers $\hat{z}$ correspond to the locations of the D local maxima of $\hat{\sigma}_C(z)$ using equation (4.19) and their reflectivities can be obtained directly from $\hat{\sigma}_C(\hat{\mathbf{z}})$. It has been shown empirically in [59] that the Capon method exhibits better performance compared to the classical Beamforming with regard to spatial resolution and sidelobe suppression. Whereas, the amplitude (reflectivity) estimate obtained by the Capon method is biased [59]. One can hence use the Least-Squares method introduced later in this chapter to estimate the reflectivity at $\hat{\mathbf{z}}$, under the hypothesis that the scatterers are well separated by the Capon spectral estimator.

4.3.3 Parametric tomographic estimators

Parametric estimators exhibit an excellent capability to discriminate scatterers located at different elevations, assuming the number of scatterers D is a priori known. Hence, after determining the number of effective sources, i.e. model order, parametric methods can be applied to estimate the spatial frequencies of the detected signals with an improved resolution, compared to nonparametric methods. Here the noise is assumed to be spatially white with components having identical variance and to be uncorrelated respect to the signals. Hereafter the Least-Squares and the MUSIC high resolution parametric methods are presented.

4.3.3.1 Least-Squares method

The LS minimization criterion for amplitude estimation presented in [59] is based on a model of multiple complex sinusoids of known frequency embedded in additive noise. This indicates that the frequencies of signals

are estimated and then put into the LS solution to obtain the corresponding amplitude estimates. Thus, the accuracy of the amplitude estimate by the LS solution relies on the accuracy of the estimated frequency. Using LS solution, one can obtain the amplitude estimate at each estimated height provided by high-resolution parametric methods.
Once the height estimates are obtained by a parametric technique, for MB-InSAR cases the LS fitting can be formulated as

$$\hat{\mathbf{s}}(l) = \arg\min_{s} \|\mathbf{y}(l) - \mathbf{A}(\hat{\mathbf{z}})s\|^2 = (\mathbf{A}^{\dagger}(\hat{\mathbf{z}})\mathbf{A}(\hat{\mathbf{z}}))^{-1}\mathbf{A}^{\dagger}(\hat{\mathbf{z}})\mathbf{y}(l) \tag{4.23}$$

where $\mathbf{s}(l) = [s_1(l), ..., s_D(l)]^T$ are the unknown complex amplitudes of D scatterers at the lth observation (look) and the steering matrix $\mathbf{A}(\hat{\mathbf{z}})$ is calculated with $\hat{\mathbf{z}}$ derived from one tomographic estimator. From equation (4.23), one may compute a L-look estimate of the reflectivity of each source using

$$\hat{\sigma_d} = \frac{1}{L}\sum_{l=1}^{L} |\hat{s}_d(l)|^2 \tag{4.24}$$

Using accurate height estimates given by parametric estimators, the LS method can provide a better amplitude estimate than nonparametric methods.

4.3.3.2 MUSIC method

The MUltiple SIgnal Classification (MUSIC) method [58] is a generalization of Pisarenko's harmonic retrieval method [51], and a parametric spatial frequency estimator for signals buried in white noise. MUSIC may be considered as a subspace-based technique as it uses a partition of the eigenstructure of the covariance matrix $\mathbf{R}$ modelled as in (4.15). Indeed the eigenstructure of $\mathbf{R}$ contains complete information on the frequencies related to $\hat{z}$ [59].
MUSIC is a subspace-based single-dimension technique, whose objective function is a measure of the orthogonality between a steering vector and

the noise subspace and is given by:

$$P_M(z) = \frac{1}{\mathbf{a}^{\dagger}(z)\hat{\mathbf{E}}_n\hat{\mathbf{E}}_n^{\dagger}\mathbf{a}(z)} \tag{4.25}$$

where $\hat{\mathbf{E}}_n$ represents the matrix of covariance eigenvectors which span the noise subspace. Once $\hat{\mathbf{z}}$, is determined by inserting equation (4.25) in the (4.19), the estimate of the complex reflectivity vector $\hat{\mathbf{s}}(l)$ can be obtained by solving a LS problem.
In [27, 59] a numerical analysis has been performed in order to compare the MUSIC methods with the Beamforming and Capon ones, demonstrating its effective better estimation results, even in presence of multiplicative noise. MUSIC performance quality depends mainly on the correlation between the scatterers. In fact, if they are fully correlated the source covariance matrix $\mathbf{R}_s$ is rank deficient and the eigenvectors belonging to the signal subspace may leak into the noise subspace.

4.4 Proposed approach and innovative aspects

As mentioned in the previous section 4.1, the main goal of the present thesis is to perform a global three-dimensional characterization and change monitoring of dense and complex urban areas. In order to achieve the aim, it has been chosen to apply tomographic SAR techniques to high resolution satellite SAR data.
In particular, the strong potentialities of the classical non- and parametric spectral estimators combined to high resolution data have been evaluated, thus the Compressive Sensing method has not been taken into account. Moreover this technique, being a sparse signal analysis, is characterize by important disadvantages as:

- difficult regularization parameter solution for the Model Order Selection (MOS) techniques

- spurious atmospheric calibration (due to the gridding problem)
- necessity to process a high number of images

The proposed approach allows to correct the geometric distortions due to the layover and to determine the information about the number of scatterers and the corresponding reflectivity within one resolution cell. The analysed AOI represents the urban area of Paris, characterized by mixed features, as vegetation, infrastructures, buildings, skyscrapers, etc. In this context, in the same resolution cell one may find the superposition of the information related to a dominant scatterer and one or maximum two others minor scatterers. For that, the maximum number of the effective sources N_0 within one resolution cell has been set to three. In order to detect, for each resolution cell, the number of the effective sources, the iterative MOS technique summarized in Fig. 4.3 has been applied to the selected estimation methods. Given a "quasi" ML solution for well separated sources, it is based on the following steps: for each resolution cell and for three iterative steps, starting from the first elevation value z_{loc} coming from the maxima local research made by means of the estimation method, a test over its intensity $P(z_{loc})$ has been evaluated as followed:

$$\frac{P(z_{loc})}{P(z_{tot})} > I_{threshold} \tag{4.26}$$

where $P(z_{tot})$ is the total intensity value and $I_{threshold}$ is the customized threshold set for the analysed AOI. If the test was positive, z_{loc} represented a real source and the process restarted in order to find the potential second or third source; if the test was negative, the process stopped.
Two different processing chains have been proposed depending on the selected estimation method. For non-parametric methods, i.e. Beamforming and Capon, the local maxima research has been performed following the proposed iterative MOS technique. For parametric methods, i.e. MUSIC, at first it has been determined a priori the number of the

sources N_S as a little bit bigger than N_0 within one resolution cell; successively, it has been applied the proposed iterative MOS technique. An important advantage of this solution is that the artefacts are not considered, due to their low intensity values.
Moreover, an innovative idea has been proposed for the 3-D change monitoring and detection of single structures. For this aim it has been necessary to perform a 3-D tomographic focalization using of Maximum-Likelihood Ratio Test (MLRT) detectors. This part will be better explained in the section 6.3.

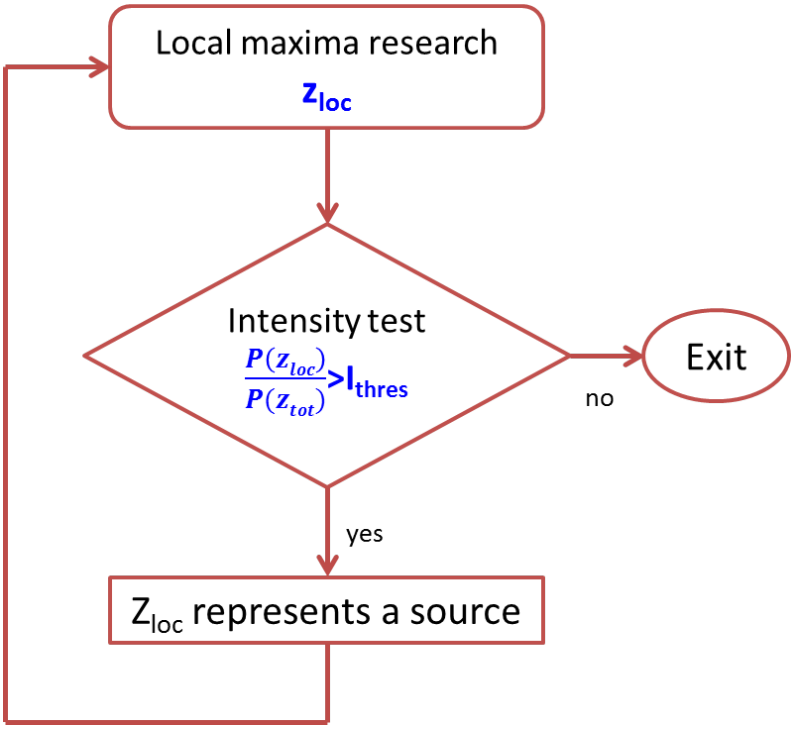

Fig. 4.3 – Diagram of the proposed approach applied to each resolution cell and for three iterative steps (three as the maximum number of the effective sources N_0)

Chapter 5

2-D analysis and results

The principal aim of the present work is to provide a global 2-D and 3-D characterization for the analysis of dense urban areas. This chapter is focused on the analysis of the quality of the processed data set, as well as for interferometric purpose and scatterers time stability, and on the extraction of tomographic 2-D second products, i.e. tomograms. Hence, an Area Of Interest (AOI) has been selected and two azimuth-profiles with different characteristics have been chosen in order to demonstrate the high potentialities for tomographic purpose of the classical estimation techniques described in section 4.3.2 and section 4.3.3. According to the well adaption of the high-resolution imagery to the remote sensing urban applications, a MB-InSAR data set acquired by the satellite TerraSAR-X in High Resolution Spotlight (HS) and SP mode over the urban area of Paris (France) has been processed.

As introduced in the previous sections, SAR imagery possesses particularly interesting features, such as foliage penetration, sensibility to scatterer shape and dielectric properties. However, SAR information over urban environments is particularly complex due to as well as the geometric distortions caused by the layover and shadowing phenomena, the complex scattering patterns within the same azimuth/range resolution cell (single/double bounce scattering, volume diffusion), the random as-

pect due to speckle effects (see section 2.2). Here a demonstration of the potentialities of TomoSAR techniques in distortion correction and in information retrieval about the number of scatterers and the corresponding reflectivity within one resolution cell is proposed in 2-D domain using basic mono-dimensional estimators as Beamforming, Capon and MUSIC. The 3-D analysis will be discussed in chapter 6.
In this context it is important to underline that the present work is mainly focused on 3-D reconstruction by very fast estimation techniques and does not take into account parsimonious signal estimators. have not been taken into account.
This chapter is structured as follow: section 5.1 reports the description and the main characteristics of the data set selected for this study; in section 5.2 the interferometric quality and time stability analysis are described; section 5.3 shows the generated 2-D tomograms.

5.1 Presentation of the data set

The analysed stack consists of 21 SP TerraSAR-X [1] images acquired in HS mode over the urban area of Paris (see Fig. 5.1) with a mean incidence angle of about 34.7° with a slant-range resolution of 1.2 m and an azimuth resolution of 1.1 m.

In Fig. 5.2a and 5.2b the spatial baseline and the spatial-temporal baseline distributions are respectively shown; the maximum elevation aperture size is about 583.5 m and the temporal baseline ranges from 24th January 2009 and 26th November 2010. It is possible to do the first considerations about the stack quality. From Fig. 5.2a it is clear that the image with ID 20 represents an outlier respect to the relative spatial baselines between the other images, whose value is about 334.4 m.

[1] I would like to acknowledge the DLR for providing TerraSAR-X data used for the present research in the frame of the project ID LAN1746

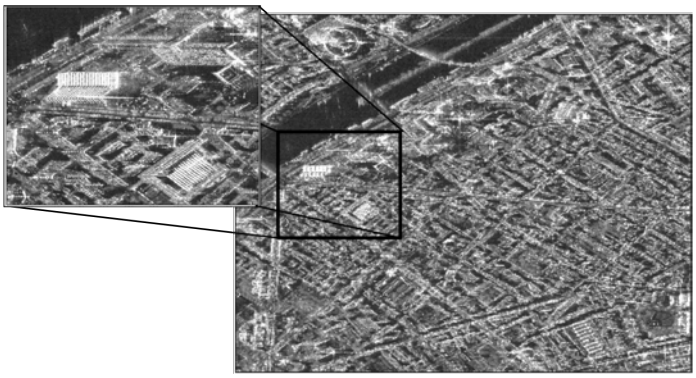

Fig. 5.1 – Multitemporal averaged amplitude image over Paris urban area derived from TerraSAR-X data stack and the selected AOI

Moreover, in 5.2b the same image is an outlier also in term of temporal baseline, together the image with ID 21 (the last one). This leads to expect, in the successive interferometric quality analysis phase, a different behaviour in term of phase component of these two images.

In order to perform the processing, an AOI containing different features, such as buildings with different dimensions and orientations, boats on the river, vegetation, has been cropped in Fig. 5.1. A subset is depicted in the top of Fig. 5.3. The area is characterized by a strong layover due to the presence of Tour Mirabeau and Tour Keller, highlighted in the figure. From the bottom of Fig. 5.3 one may appreciate the geometric distortion effect: taller buildings within the subset are 'lying down' onto the ground along the range direction, showing both their roofs, façades and bases interfering with scatterers situated below them. This phenomenon may be better figured out looking Fig. 5.4 where a simplified map of the selected subset taken from [2] is reported. Here the Tour Keller's shadow covering part of the Tour Espace 2000, Tour Perspective 2 and the ground could be seen as the layover induced by the main skyscraper over the other twos. Hence, structure parts and ground covered by the shadow may be imaged in the SAR resolution cell together to the Tour Keller ones because of the layover. In the following, we will refer to the

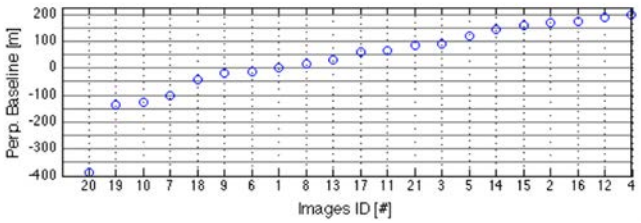

(a) Perpendicular baseline distibution

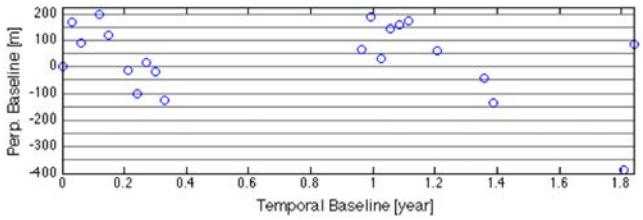

(b) Spatial-temporal baseline distribution

Fig. 5.2 – Distributions of the 21 acquisitions in the spatial and temporal baseline domains

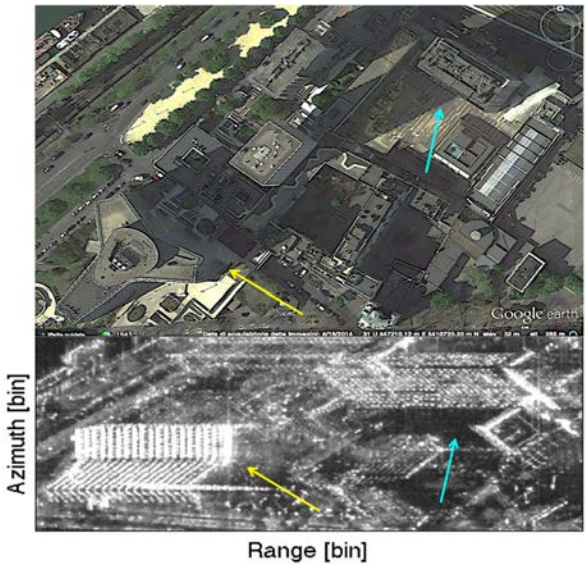

Fig. 5.3 – Image taken from Google Earth (top) and multitemporal averaged amplitude image derived from TerraSAR-X data stack (bottom)

skyscrapers indicated by the yellow and turquoise arrows in Fig. 5.3 as, respectively, Tour Mirabeau and Tour Keller.

Fig. 5.4 – Semplified map taken from [2] of the selected subset of the AOI

5.2 Interferometric quality and temporal stability analysis

A first step for the tomographic processing is the analysis of the interferometric quality of the data to be used. First of all the attention goes to the accuracy of the co-registration phase. The images, being acquired from different (even though slightly) point of view at different distances, need to be rotated, shifted and scaled relative to the *master* in order to align the samples for phase differencing. A sub-pixel registration of all the focused SAR images is strictly required for interferometric processing whose quality is highly dependent on co-registration accuracy. Consequently, a good coherence between images as well as a good noise phase reduction, mainly due to the atmospheric and flat earth components (see section 3.2), highly impact the quality of the secondary products as the tomograms and the DSMs. Here, starting from a co-registered and flattened data set, a calibration of the atmospheric phase component has been applied to the signals, treating the problem as a low-pass filtering one. The analysis has been performed considering all the combinations

of two images out of the stack, that is $\frac{N \cdot (N-1)}{2}$ samples (with N the number of processed images).

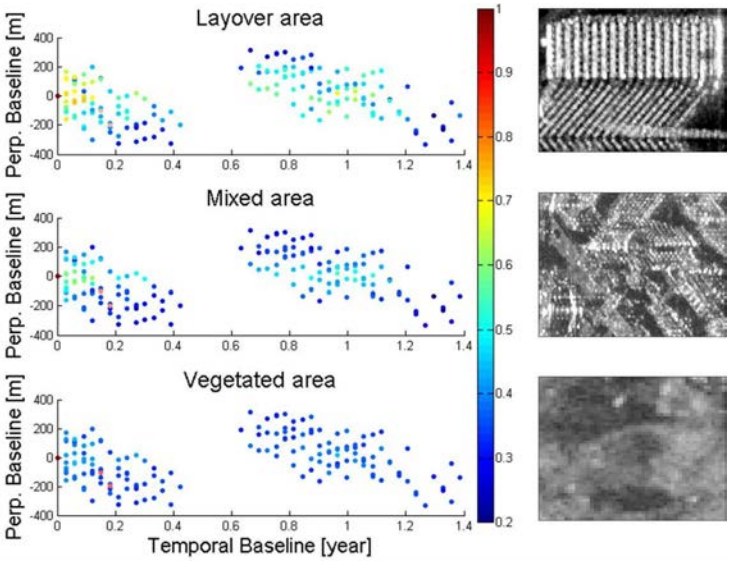

Fig. 5.5 – Spatial-temporal trend of coherence mean values (left) evaluated over different image subsets (right) considering the first 19 (good) images within the stack

In Fig. 5.5 (left plots) it is represented the mean coherence values evaluated respect to the spatial and temporal baselines. Several image subsets characterized by different scenes, such as layover, mixed and vegetated areas, have been cropped and showed in Fig. 5.5 (right tiles). As expected, the highest coherence values are related to the area characterized by layover induced by the Tour Mirabeau, whereas the lowest ones are related to the area mostly covered by vegetation. Moreover, the coherence increases especially for the layover area decreasing the spatial baselines values.

From Fig. 5.6 one may better appreciate the globally interferometric quality trend over the stack. In particular, in Fig. 5.6a and 5.6b the calibrated coherence maps evaluated along both the increasing temporal

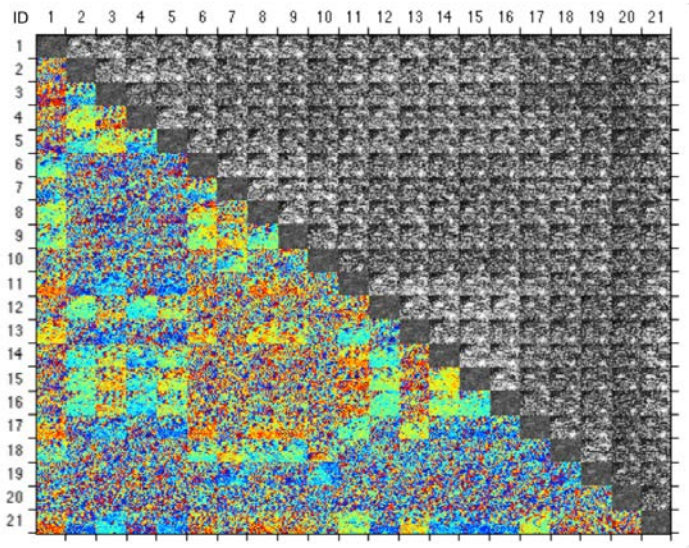

(a) Increasing temporal baseline

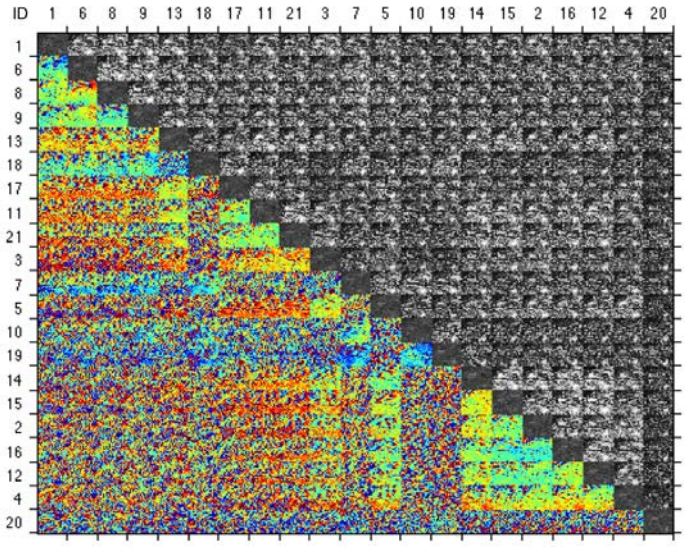

(b) Increasing spatial baseline

Fig. 5.6 – Calibrated coherence maps along temporal and spatial baselines

and absolute spatial baselines are reported. Amplitude images (principal diagonal), coherence images (upper triangular part) and flattened and calibrated interferograms (lower triangular part) computed over the en-

tire processed stack are depicted. Both figures show the trend of the interferometric phase quality for all the combinations of two images out of the stack. As anticipated, image with ID equal to 20 results highly uncorrelated with all other images most probably because it presents both the higher spatial baseline value (about -386.7 m) and a dispersed acquisition date (see Fig. 5.2a and 5.2b). On the other hand, pair images with small baselines are characterized by a higher correlation presenting better and brighter coherence images. Interferometric phase quality, and consequently tomographic elevation resolution, strongly depends on temporal and spatial baseline characteristics. Indeed, as depicted in Fig. 5.6b, the global interferometric quality increases with decreasing spatial baseline values, i.e. moving from the upper-right and lower-left corners of the matrix to the principal diagonal. In Fig. 5.7 it is reported a particular of the coherence map and the interferogram between images whit IDs 1 and 2, obtained applying the Lee filtering with a window equal to 9. Fig. 5.7a represents the coherence values (ranging from 0.3 to 1) that appear very high (bright pixels) for the man-made features, such as the buildings, and very low (dark pixels) for natural environments like the river (upper-left). Fig. 5.7b represents the flattened, calibrated and filtered interferogram between the same interferometric pair and one may note how areas characterized by low coherence show random phase pattern whereas more correlated features are characterized by more regular pattern and phase of the features whose height is higher than h_{amb}, as ones affected by the layover, are wrapped every 2π phase cycle.
Above results highlight the high coherence level between the majority of the images within the stack, confirming the effective capabilities of TSX high resolution data. On the basis of these preliminary analysis the two (temporally) last images have been discarded and the experimental results have been achieved processing the leftover 19 images.

In order to deeply describe the urban AOI, a time stability analysis of the

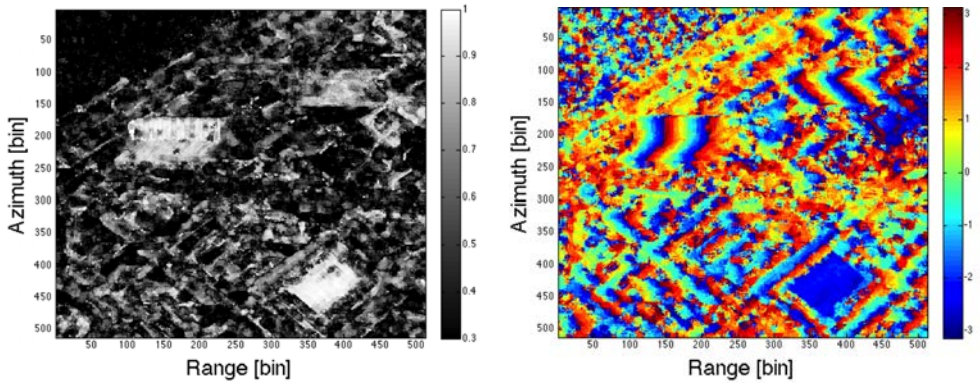

(a) Filtered coherence image (b) Filtered interferogram image

Fig. 5.7 – Coherence image and interferogram computed between images with IDs 1 and 2

signals have been carried out adapting to the SP data two statistical descriptors related to the signal stationary aspect and coherence presented in [20, 31] for Polarimetric SAR (PolSAR) data based on Maximum Likelihood statistic test. There a PolSAR multidimensional information is analysed using a linear time-frequency decomposition which permits to detect man-made structures and ships and to describe their polarimetric behaviour for different azimuth angles of observation and frequencies of illumination.

The 2-D temporal coherent stability between the $\{s_j\}_{j=1,j\neq i}^{19}$ signals has been computed accordingly to the indicator ρ_T given by

$$\rho_T = 1 - |\hat{\mathbf{R}}|^{1/N} \tag{5.1}$$

where $\hat{\mathbf{R}} = \underline{\mathbf{P}}\mathbf{R}\underline{\mathbf{P}}$, with $[P]_{ii} = diag(\sqrt{\mathbf{R}_{ii}^{-1}})$. Its values range from 1 (maximum correlated case) and 0 (decorrelated case). In Fig. 5.8a its trend shows (and confirms) that natural environments such as the river in the upper right part of the images have low ρ_T values. On the contrary, coherent reflectors like man-made targets and buildings show the highest values of ρ_T especially over the squared lower-left roof.

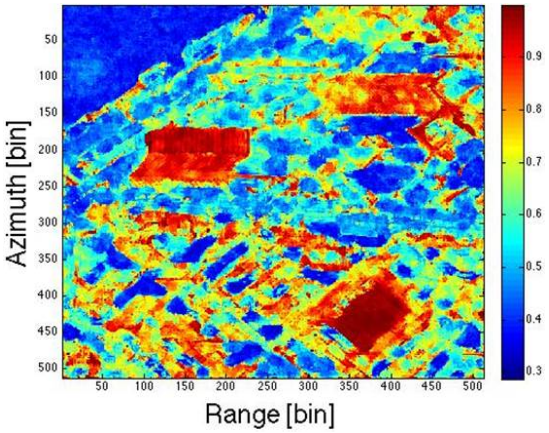

(a) Coherence indicator

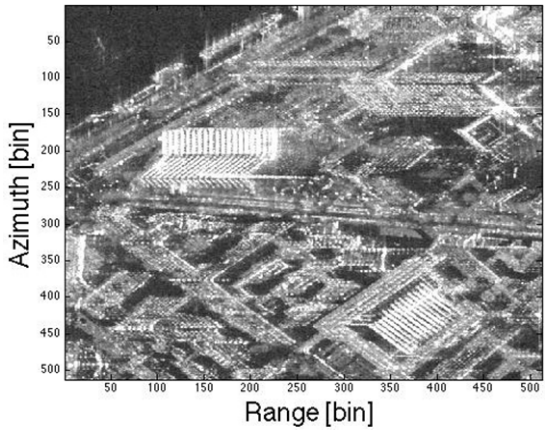

(b) Multitemporal averaged amplitude image

Fig. 5.8 – Coherence indicator trend over the selected subset ranges from 1 (high coherence) and 0.3 (low coherence) and relative amplitude image (right)

The 2-D temporal incoherent stability characterization has been assessed over the data stack by testing the fluctuation of the intensities $\{I_i(x,y)\}_{j=1,j\neq i}^{19}$ of the signal computing the parameter Λ by the equation (5.2)

$$\Lambda = \frac{\prod_{i=1}^{N} \mathbf{I}_i^{\frac{1}{N}}}{\frac{1}{N}\sum_{i=1}^{N} \mathbf{I}_i} \tag{5.2}$$

where $\mathbf{I}_i$ represents the intensity matrix of the ith image.

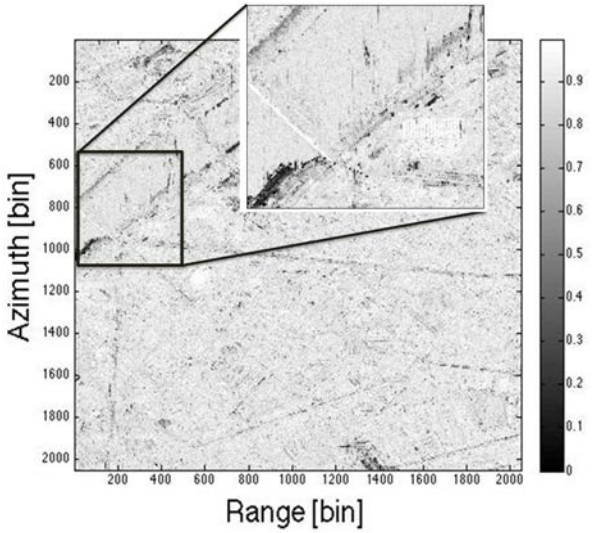

(a) Parameter Λ

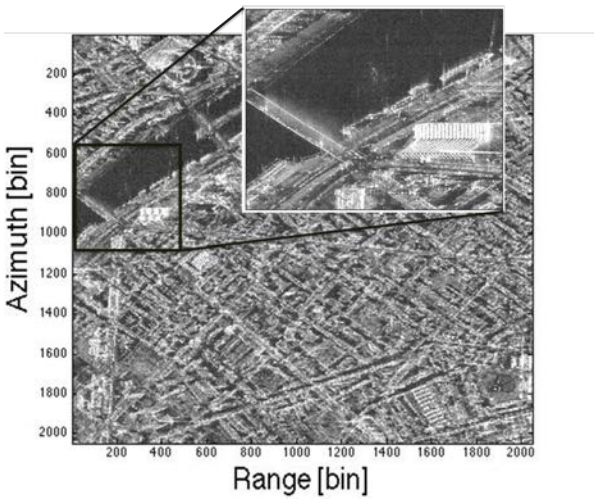

(b) Multitemporal averaged amplitude image

Fig. 5.9 – Image of the parameter Λ on Paris test site, whose values go from 0 (very low stationarity) and 1 (very high stationarity)

The relative image over all the test site is represented in Fig. 5.9: not

moving features like buildings and bridges show high Λ values, whereas boats and cars over main streets are affected by a very low stationary behaviour. These results show the capability of these indicators to provide complementary information, adapted to the case of man made environments.

5.3 Tomograms generation

SAR tomography can be derived from the data covariance matrix $\hat{\mathbf{R}}$ in the frame of a classical problem of spectral estimation using mono- and multi- dimensional methods. These approaches determine $\hat{\mathbf{z}}$, an estimate of the elevation of the scatterers under observation, as the coordinates of the $\hat{n}_s$ largest local maxima of a continuous objective function $P(z)$, $\hat{\mathbf{z}} = argmax P(z)$. In this section SAR tomographic results have been achieved implementing and applying different mono-dimensional estimators over the data set already described in section 5.1. 2-D tomograms have been generated over several azimuth profile in order to estimate building heights and to distinguish different scatterers within the same resolution cell. In particular the following mono-dimensional methods have been used: Beamforming and Capon, non-parametric approaches generally used to globally appreciate the structure of a volumetric medium; MUSIC, parametric approach generally characterized by better resolution and performance for the analysis of discrete sources and affected by data modelling errors. Regarding the estimation of the MUSIC pseudo-spectrum, the signal subset dimensions N_S has been set equal to 4, accordingly to the hypothesis on the basis of the proposed approach (see section 4.4).
Tomograms illustrated in Fig. 5.10b and 5.10c are referred to the relative image profile highlighted in Fig. 5.10a by the red line and they reflect the high quality resolution of the processed data. Indeed, it is evident how also with basic and classical spectral estimation models it is pos-

sible to reconstruct building shapes and profiles. Focusing attention on slant range tomograms shown in Fig. 5.10b, moving from the top to the bottom one may note the effective vertical resolution improvement between the different approaches: sidelobes, probably due to atmospheric phase noise residuals, are particularly strong for Beamforming estimations, strongly reduced by Capon and completely resolved by MUSIC approach. From ground range normalised results depicted in Fig. 5.10c, one may appreciate the effective reconstruction of buildings shapes and the strong correction of the distortions due by the layover. Main vertical profiles may be clearly perceived thanks to the strong double bounce scattering responses related to the wall-ground interaction, as well as on the whole top of the relevant last building located at about 20 m over the referencing zero ground height.

Tomograms illustrated in Fig. 5.11 are referred to the image profile highlighted in Fig. 5.11a by the red line and strongly characterized by the geometric distortions related to the layover induced by Tour Keller. Thanks to the high quality resolution of the processed data, it is possible to distinguish, for some resolution cells, more than one intensity local maxima. These peaks are related to different scatterers due mainly to the skyscraper features and the ground as depicted in the relative scheme on the right of the tomograms. In particular from Fig. 5.11b it is possible to detect two scatterers, corresponding for example to the ground and the building façade. In Fig. 5.11b one may appreciate the presence of up to three scatterers within the same resolution cell due, for example, to the addition of the building roof. This represents a valuable capability of tomographic techniques that allows to obtain complete point clouds and, hence, complete DSMs. This aspect will be better analysed in chapter 6. Especially for MUSIC results (bottom tomograms in Fig. 5.11b and 5.11c), one may appreciate how thanks to the proposed approach, the artefacts are not taking into account as real sources, thanks to their low intensity values. Furthermore, the presence of artefacts has been

strongly reduced filtering the signal by means of two masks obtained by a threshold computed on the parameter ρ and Λ described in the previous section 5.2. From the tomograms obtained by the MUSIC approach one may note how the hypothesis to set the number of the sources N_S equal to 4, i.e. as a little bit bigger than $N_0 = 3$, allows to achieve very good results in terms of vertical resolution and accuracy and source detection.

Results reported in the present chapter have demonstrated the possibility to perform dense urban area 2-D analysis using tomographic techniques and high resolution satellite SAR data. Exploiting mono-dimensional spectral estimation models, the buildings heights estimation and the scatterers number extraction have been carried out. In this way it has been possible to resolve pixels affected by the layover distinguishing up to three scatterers within the same resolution cell. On the basis of these conclusions a 3-D characterization has been performed over the same subset, whose results are presented in the following chapter.

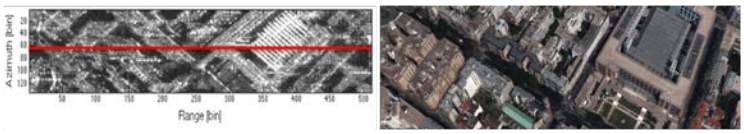

(a) Amplitude and Google Earth image of the analysed profile highlighted in red over the AOI

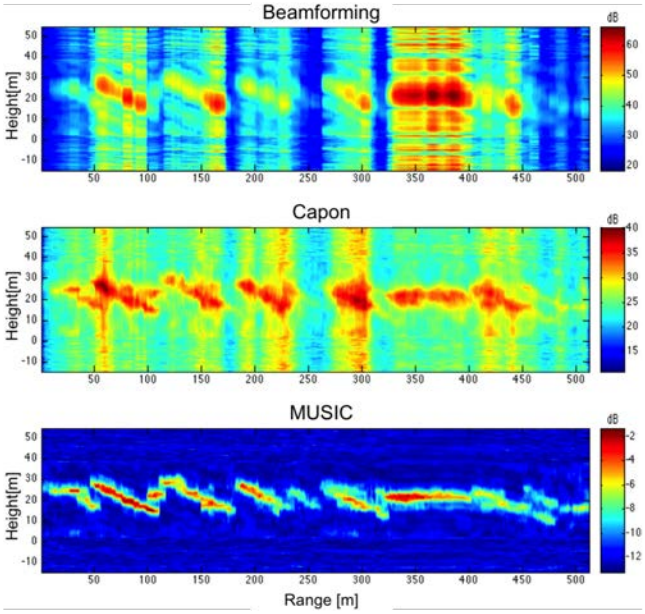

(b) Slant range reflectivity tomograms

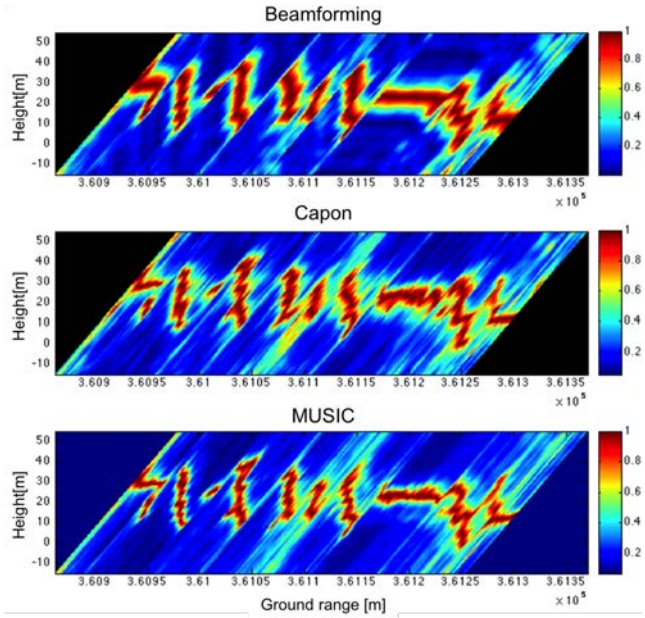

(c) Ground range normalised reflectivity tomograms

Fig. 5.10 – Tomograms generated over one profile applying Beamforming, Capon and MUSIC spectral estimators

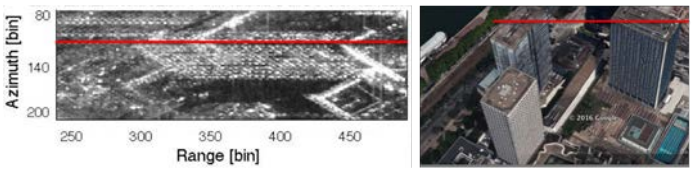

(a) Amplitude and Google Earth image of the analysed profile highlighted in red over the AOI

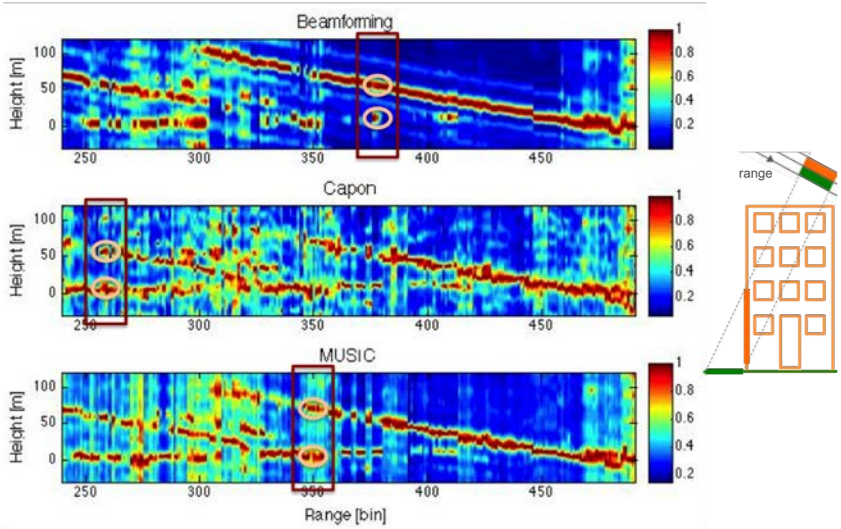

(b) Slant range normalised reflectivity tomograms: 2 detected scatterers

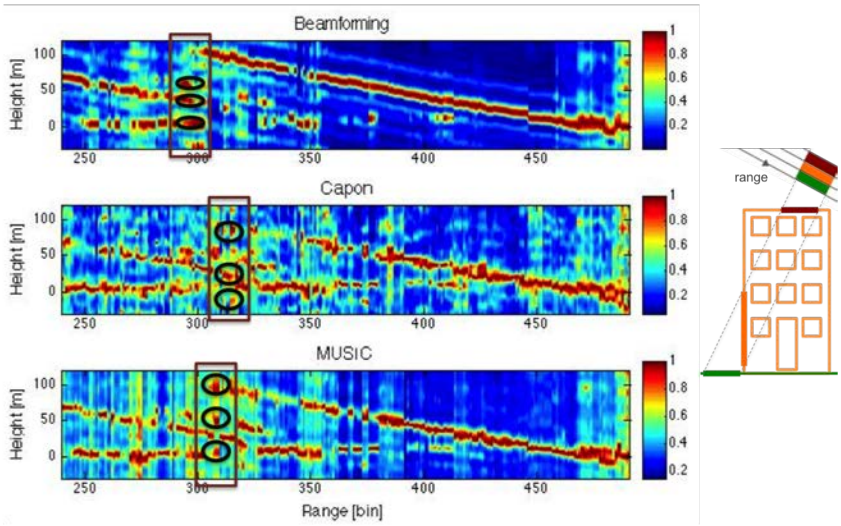

(c) Slant range normalised reflectivity tomograms: 3 detected scatterers

Fig. 5.11 – Tomograms generated over one layover-affected profile applying Beamforming, Capon and MUSIC spectral estimators

Chapter 6

3-D analysis and results

In the present chapter a global 3-D characterization of dense and complex urban areas exploiting SAR tomographic techniques is presented. In this sense, several reconstructions in terms of building height, vertical reflectivity and time stability have been carried out processing an adequate set of multitemporal high resolution TSX images in order to deeply analyse build-up areas. Starting from experimental results obtained in the previous chapter, here the study has been widened to the urban azimuth/range tiles depicted in Fig. 6.1. In particular, Fig. 6.1a includes the azimuth-profile analysed in Fig. 5.10a and contains a mixed scenario characterized by residential buildings, streets, vegetation; 6.1b shows the tile including the Tour Keller (previously analysed in 5.11a) and it is evident its strong layover along the range direction; 6.1c represents the Tour Mirabeau, a skyscraper composed of three branches forming a triangular island. In the following sections different investigations are presented in term of built-up area and single building 3-D reconstruction and characterization. Moreover, the 3-D views have been reconstructed in ground range processing the results obtained considering up to three scatterers within one resolution cell and Beamforming, Capon and MUSIC approaches. The investigation have been carried out for three different intensity levels, in each of which the maximum abso-

lute reflectivity value has been identified from the spectrum evaluated for each resolution cell within the tile. The obtained products have led to focus the attention over the ones extracted by means of the MUSIC method. Furthermore, results shown hereafter have been preprocessed applying several filters in terms of temporal coherent and stable scatterer analysis, in order to not consider strongly unstable pixels, e.g. cars over the main streets, that might add noisy information.
Hence, tiles analysed in the following have been chosen in order to demonstrate different capabilities of tomographic techniques. In particular, single building height reconstruction and layover correction are demonstrated in section 6.1 for different man-made features, showing the extracted point clouds from different point of views; in section 6.2 the estimation of vertical building reflectivity is presented; section 6.3 shows the results coming from an innovative scatterers time stability analysis.

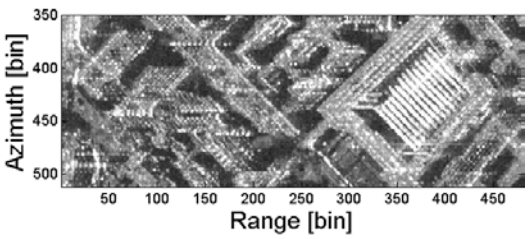

(a) Tile over a mixed urban area

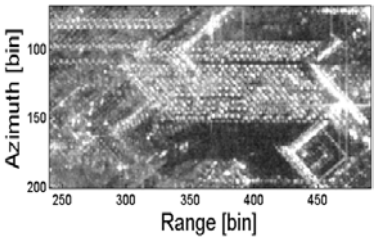

(b) Tile including Tour Keller

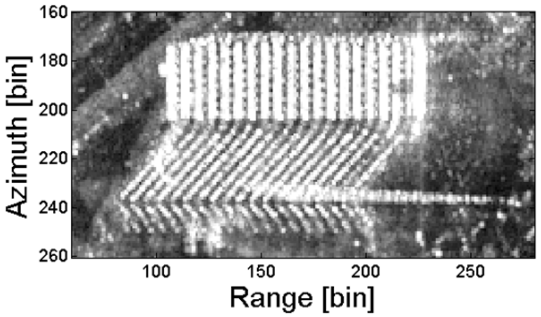

(c) Tile including Tour Mirabeau

Fig. 6.1 – Tiles considered for 3-D reconstructions and investigations

6.1 Height map generation

As mentioned in chapter 3, TomoSAR is a valuable technique for the extraction of the height information of a selected area/feature. In order to operate in the 3-D field, the 2-D spectral analysis described in section 5.3 for an azimuth profile is widened to the azimuth/range resolution cells within the selected tile. This process leads to the generation of sparse point clouds that, from the computational point of view, may be considered like an ASCII file in which the height values are listed in addition to the horizontal coordinates of the m detected points (sometimes up to hundreds of thousands). In this context it is important to introduce the concept of completeness and accuracy. The completeness indicates a homogeneous data distribution on the entire studied area, to minimize the zones with poor or any information. The accuracy is the standard deviation of the elevation data differences between the model surface and a referring surface.
In this section several point clouds are reported for tiles (see Fig. 6.1) characterized both by mixed features, such as man-made structures and vegetation, and by layover distortions. The 3-D views have been reconstructed in ground range coordinate system starting from results obtained considering up to three scatterers within one resolution cell and Beamforming, Capon and MUSIC approaches.
Starting from Fig. 6.2, results obtained using Beamforming, Capon and MUSIC approaches over a tile including the first profile analysed in section 5.3 (Fig. 5.10a) are depicted. As one may note, the height map extracted by Capon method appears to be sparser and noisier, whereas the Beamforming and the MUSIC ones show tidier point clouds. Moreover, as reported in table 6.1, point clouds generated using MUSIC approach are characterized by a higher rate of completeness (in particular the $\sim 4.8\%$ and $\sim 5.5\%$ more of detected points than, respectively, Beamforming and Capon methods). Focusing the attention on the MUSIC

Mixed urban area

Scatterers order	Beamforming	Capon	MUSIC
I	52 469 (~97.8%)	52 465 (~98.55%)	52 870 (~93.7%)
II	1 122 (~2.1%)	741 (~1.40%)	3 450 (~6.1%)
III	53 (~0.1%)	22 (~0.04%)	83 (~0.2%)
ALL	53 644 (100%)	53 228 (100%)	56 403 (100%)

Single building: Tour Mirabeau

Scatterers order	Beamforming	Capon	MUSIC
I	10 975 (~98.3%)	10 777 (~96.8%)	11 020 (~95.0%)
II	164 (~1.5%)	244 (~2.2%)	478 (~4.1%)
III	25 (~0.2%)	117 (~1%)	104 (~0.9%)
ALL	11 164 (100%)	11 138 (100%)	11 602(100%))

Layover area: Tour Keller

Scatterers order	Beamforming	Capon	MUSIC
I	19 840 (~93.3%)	18 973 (~88.0%)	19 623 (~84.9%)
II	1 229 (~5.8%)	1 610 (~7.5%)	3 103 (~13.4%)
III	196 (~0.9%)	982 (~4.5%)	392 (~1.7%)
ALL	21 265 (100%)	21 565 (100%)	23 118 (100%)

Table 6.1 – Amount of the scatterers detected at three levels using different estimation techniques over several tiles

products, in Fig. 6.3 results obtained considering separately the dominant, the second and all the detected sources are reported. The analysed area, underlined by the red lines in Fig. 6.3a, is characterized by several residential buildings and a big almost squared structure defined by different features. Fig. 6.3b, 6.3c and 6.3d show the 3-D height maps generated considering, respectively, all the estimated scatterers, only the dominant (first) sources and the second ones. Comparing the 3-D views with the simplified 3-D map in the top of the figure, one may perceive the reconstruction of the main building shapes and location and the streets orientation. Especially for the big squared structure, considering all the detected sources one may recognize the principal features, such as the external wall, the internal edifice and the external patio. It is also evident that the main information is given by the dominant scatterers, even though second sources give a contribution mainly for scatterers at lower

height. It is important to underline that elevation values represented in the height map and pointed out in figure legends appear to be coherent with the one estimated from Google Earth.

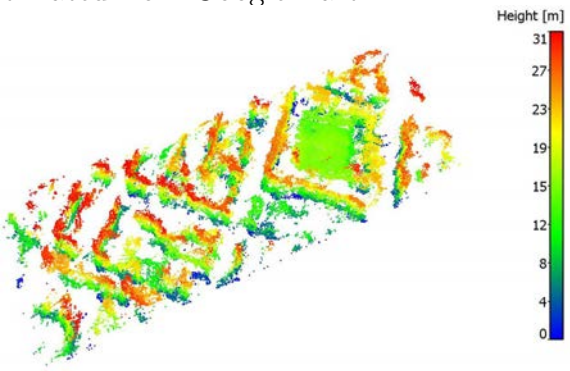

(a) All detected sources: Beamforming

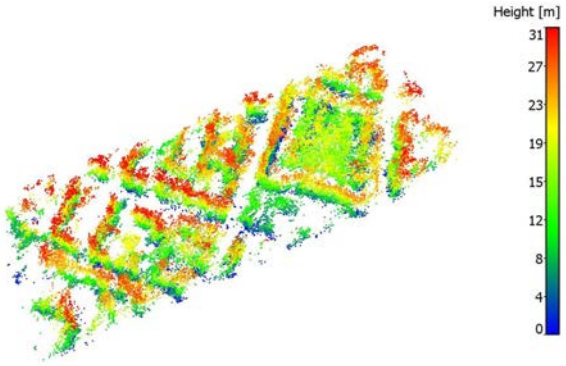

(b) All detected sources: Capon

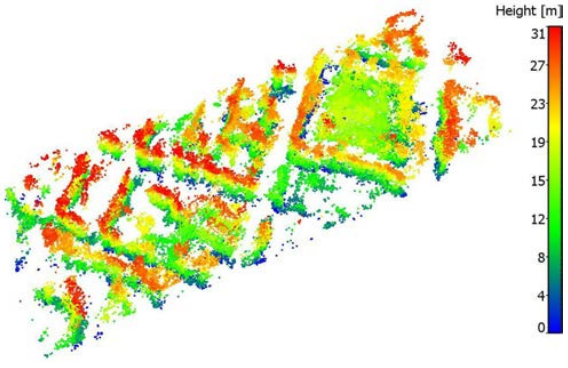

(c) All detected sources: MUSIC

Fig. 6.2 – 3-D height maps represented in ground range over a mixed urban area using Beamforming, Capon and MUSIC approaches and considering all the detected sources

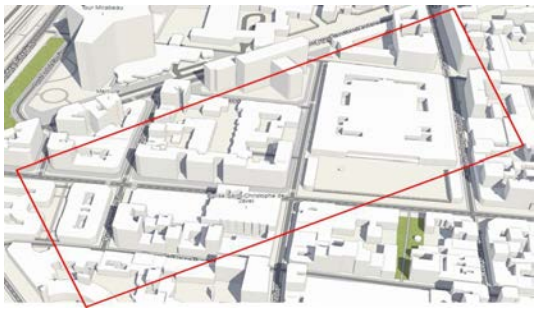

(a) 3-D map of the selected tile

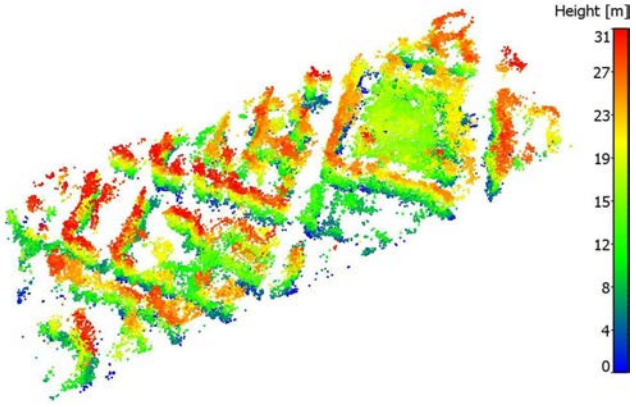

(b) Dominant, second and third detected scatterers

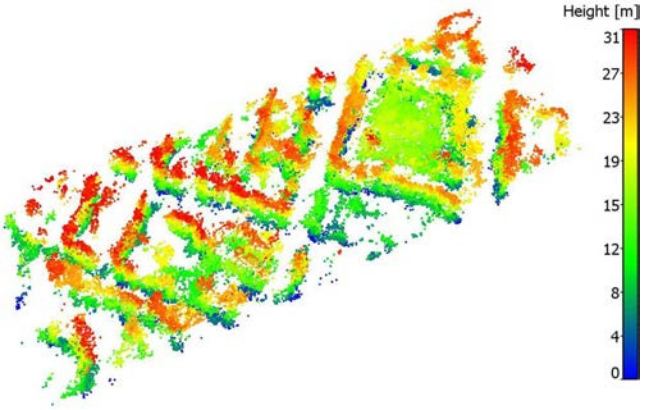

(c) Dominant scatterers

(d) Second detected scatterers

Fig. 6.3 – 3-D height maps represented in ground range over a mixed urban area considering several detected scatterers using MUSIC method

The main interesting capability of TomoSAR is the layover distortion correction, that is detecting and distinguishing different scatterers with different elevation imaged together in the same range/azimuth resolution cell of the SAR image. In order to demonstrate it, the Tour Keller layover imaging over the Tour Espace 2000 and the Tour Perspective 2 has been taken into account (the effect is well visible in Fig. 6.1b). Fig. 6.4a reports the front and top (simplified) map views that if compared with, respectively, Fig. 6.4b and Fig. 6.4c gives an additional confirmation of the potential of this technique combined with high resolution satellite SAR data. Focusing on the biggest skyscraper, one may perceive its shape and the location of its two façades. Moreover, it is clear that resolution cells affected by layover have been georeferenced and the information related to features below them has been partially reconstructed in the others two main buildings and the ground. It is also interesting make a comparison between Fig. 6.4d and Fig. 6.4e where relative detected scatterers are highlighted respect to the point cloud populated by all the estimated sources (imaged in gray). One may note how the majority of the second source (that consists in about the 13.4% of the total detected points) are related to pixels affected by the layover, that is scatterers related to a relative peak in the reflectivity spectrum.
Eventually, in order to perform the investigation of a single building reconstruction the Tour Mirabeau has been selected, thanks to its particular shape (as one may note in Fig. 6.6a) and strong layover distortions. In this case the layover induced by the structure does not involve other important features but the ground. Hence several views of merely the point cloud extracted considering all the detected sources are represented. Fig. 6.5 shows all the scatterers detected using the three considered spectral estimation techniques. Even here Capon products reveal a noisy behaviour: the building shape is not clear and there are several sparse points within the scenario.

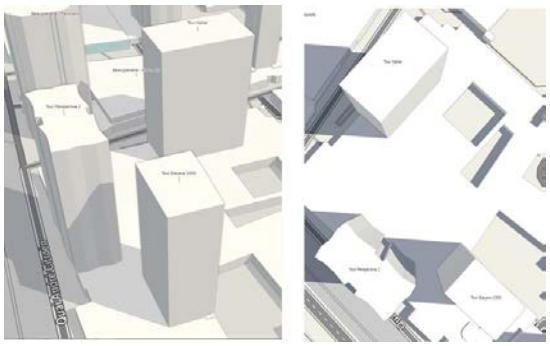

(a) 3-D views of the Tour Keller's area

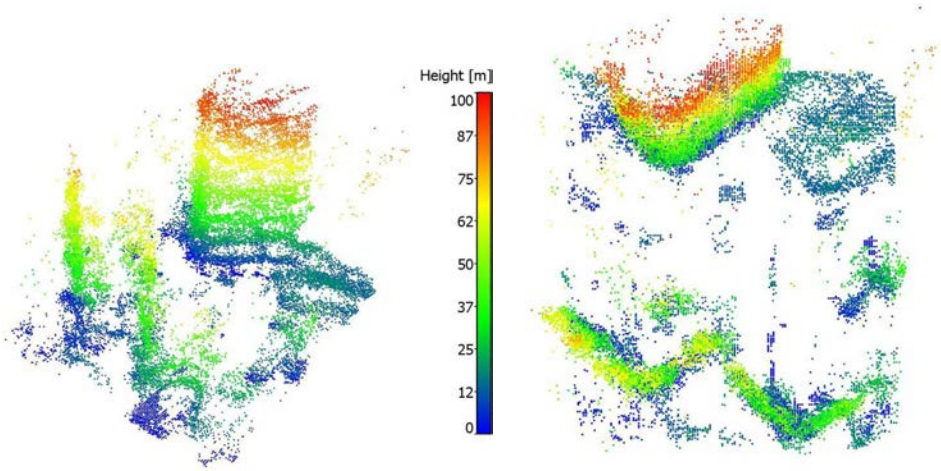

(b) All detected scatterers: front view (c) All detected scatterers: top view

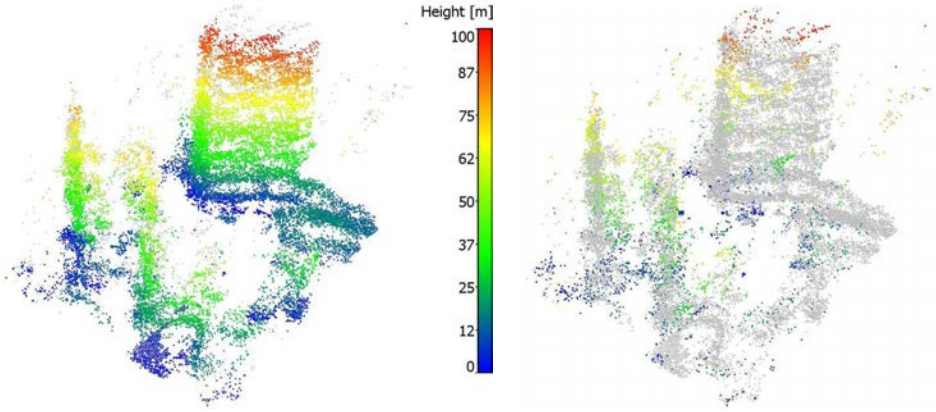

(d) Dominant detected scatterers (e) Second detected scatterers

Fig. 6.4 – 3-D height maps of Tour Keller area represented in ground range and extracted considering several detected scatterers using MUSIC method: layover distortions have been mostly corrected

On the contrary, the point cloud extracted by means of the Beamforming and showed in Fig. 6.5a reveals clearly the particular shape and intersection of the two façades and their elevation. MUSIC results depicted in Fig. 6.5c seem to lose information about the wall, especially at the top, adding however information about the roof of the structure (better highlighted in Fig. 6.6). Moreover, from the table 6.1 it is clear that this method allows to detected more points lying under the layover than the other two. For these reasons we focused on the MUSIC products. Comparing the top view in Fig. 6.6b with the right one in Fig. 6.6a one may note the good reconstruction of the particular shape of the two façades facing the radar signal. At the same time the frontal view depicted in Fig. 6.6c show the point detection at the different height, reconstructing partially the roof of the building. Moreover pixels imaged in layover are quite geometrically corrected and georeferenced in relation to the others demonstrating the extraction of the form of the global building. Nevertheless, ground involved by the layover has been reconstructed for a very small part, showing anyway the limits of this technique.
Globally, the proposed 3-D views show good results in terms of reconstruction of the shape and the location of man-made target and in elevation retrieval. The point clouds appear slightly noisy, i.e. some scatterers appear to have wrong elevation and/or location. It is probably due to residual errors related to the coregistration and calibration signal steps and to residual unstable scatterers coming form the pre-processing filtering applied to the point clouds. In particular, the Capon method has led to point clouds noisier and sparser respect to the others; products obtained by means of Beamforming technique ; the MUSIC approach was found to be the better in terms of layover correction and point cloud completeness. Indeed, with respect to the Capon and Beamfoming, a higher number of points related both to the total detected sources and to the second and third ones (see the statics in table 6.1) have been detected, showing the higher capabilities in scatterers detection at different

reflectivity level within the same resolution cell. Further, this is congruent with the 2-D investigations performed in section 5.3, where it has been shown the MUSIC superior capability in sidelobes reduction and accuracy estimation.

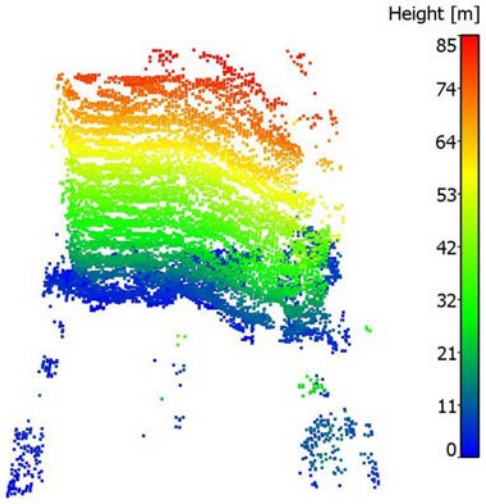

(a) All detected scatterers: Beamforming

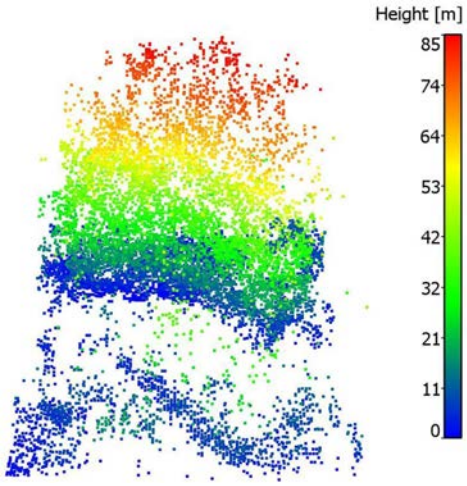

(b) All detected scatterers: Capon

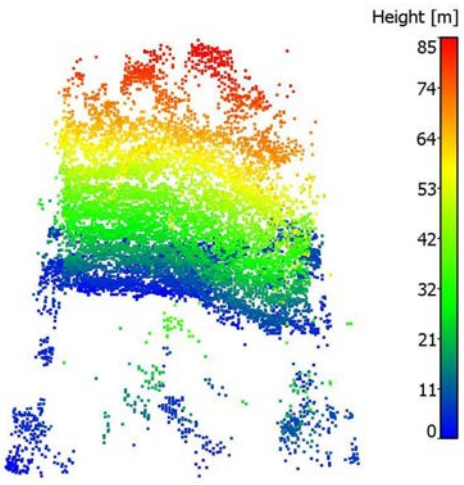

(c) All detected scatterers: MUSIC

Fig. 6.5 – 3-D height maps of Tour Mirabeau represented in ground range and considering results obtained using Beamforming, Capon and MUSIC approaches

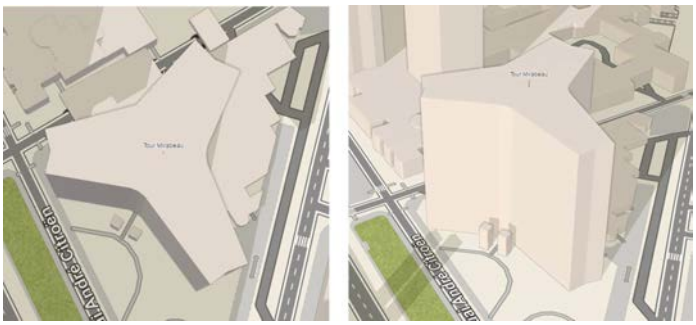

(a) 3-D views of the Tour Mirabeau

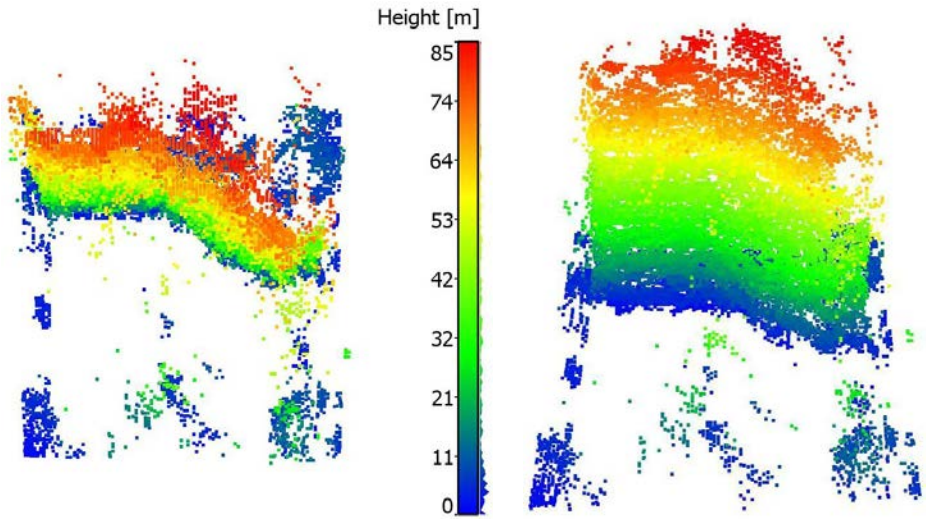

(b) All detected scatterers: top view

(c) All detected scatterers: front view

Fig. 6.6 – 3-D height maps of Tour Mirabeau represented in ground range and from different point of views and obteined using the MUSIC method

6.2 Vertical reflectivity estimation

Another important characterization of the built-up areas consists in the estimation of the vertical reflectivity information. For ground imaging, the reflectivity may be modelled as the superposition of the echoes from a large number of uncorrelated scatterers randomly dispersed through the

resolution cell. Hence it is expected to be characterized by low reflectivity values. For building imaging, the reflectivity is supposed to be higher at the wall-ground interaction where typically occurs the double bounce reflection. It is important to restate that the reflectivity profile is used to estimate scattering parameters, such as the number of scatterers in a pixel, their elevations, and their reflectivity strength. Here it has been decided to focus on the analysis of the Tour Keller and Tour Mirabeau areas, due to their high elevation spread.

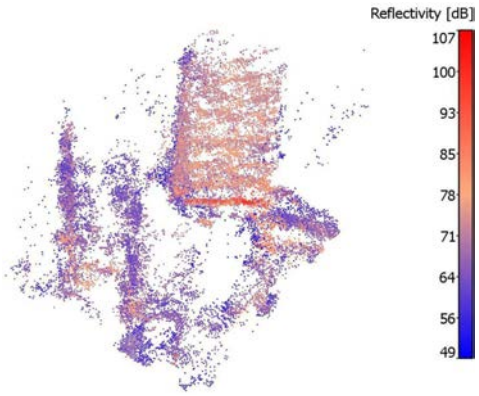

(a) All detected scatterers

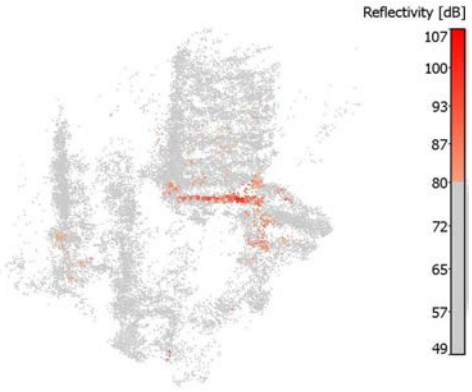

(b) All scatterers: filtering lowest values

(c) Dominant detected scatterers

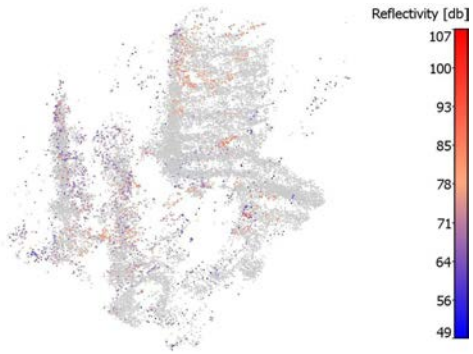

(d) Second detected scatterers

Fig. 6.7 – 3-D reflectivity maps of the Tour Keller area represented in ground range and extracted considering several detected scatterers. Highest values are related to the double bounce reflection occurring at the wall-ground interaction

Fig. 6.7 represents the reflectivity maps evaluated at different point detection steps for Tour Keller area. Fig. 6.7b show points characterized by high reflectivity value, considering all the detected sources. It is evident that these points are located at the basis of the main buildings due to the strong double bounce reflection occurring at the wall-ground interaction. On the other side the ground, accordingly with the expectations, is characterized by lower reflectivity values (see Fig. 6.7a). Moreover, from the histograms in Fig. 6.8 one may note how the majority of the scatterers with high reflectivity values (i.e. $>= 80$ dB) have been detected at the first step, i.e. for the dominant scatterers. This is congruent with the assumptions set for the detection of the sources at the different reflectivity levels.

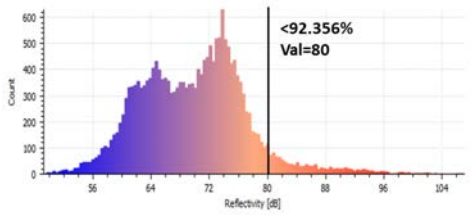

(a) Dominant detected sources

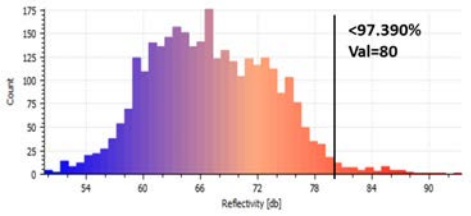

(b) Second detected sources

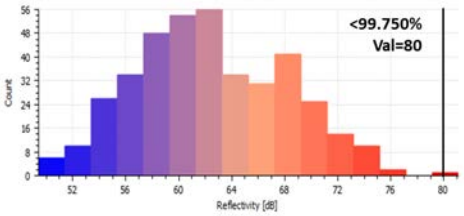

(c) Third detected sources

Fig. 6.8 – Tour Keller area: reflectivity histrograms for different detected sources

Regarding the Tour Mirabeau structure, Fig. 6.9a and 6.9b underline the double bounce effects at the wall-ground interaction, revealed by the presence of scatterers characterized by the highest reflectivity. Moreover

Fig. 6.9a shows mean reflectivity values in correspondence of the roof of the building, probably related to the correlated surface scattering.

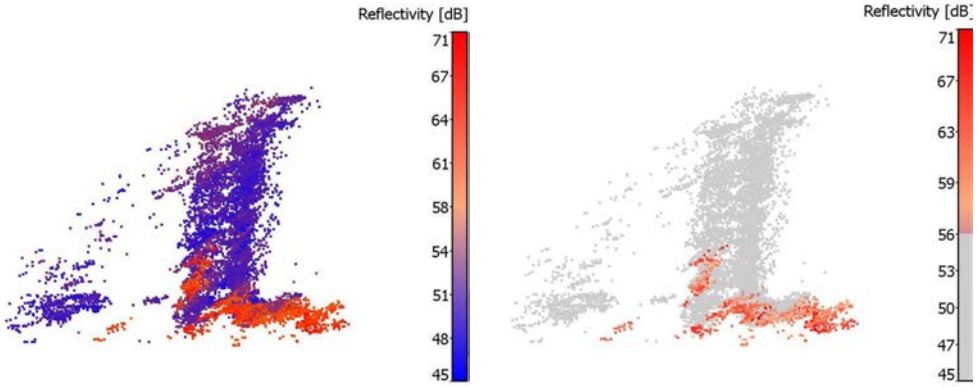

(a) All detected scatterers

(b) All detected scatterers: filtering lowest values

Fig. 6.9 – Reflectivity maps of the Tour Mirabeau represented in ground range and extracted considering all the detected scatterers. Highest values are related to the double bounce reflection occurring at the wall-ground interaction

6.3 Time stability analysis

The main goal of the present work is to perform a global and 3-D characterization of built-up areas using tomographic techniques and high resolution satellite SAR imagery. In this sense, in the previous sections results in terms of height map extraction and vertical reflectivity estimation have been presented over different tiles. In the present section it is presented an innovative 3-D time stability analysis of the observed scene, aimed to identify unstable detected scatterers and processed images from the time point of view.

The basic idea is to evaluate a set of 3-D intensities

$$I_{i(x,y,z)} \quad \text{with} \quad i = 1, \ldots, N_{im} \tag{6.1}$$

discarding for each step the current image, that means consider the signals

$$\{s_j\}_{j=1,j\neq i}^{N} \quad \text{with } N \text{ the image number} \tag{6.2}$$

of the $N-1$ 2-D images. Since these 3-D intensity estimates have similar resolution properties, the variations with i permit to appreciate the importance of the missing image. The temporal stability at coordinates (x, y, z) can then be measured using a Modified Coefficient of Variation[1], CVm, derived from the set of intensities

$$\{I_{i(x,y,z)}\}_{i=1}^{N_{im}} \tag{6.3}$$

Fig. 6.10a plots an extraction of the most perturbing image contributions varying the number of discarded images and the number of the unstable pixels at the different steps, i.e. discarding always one more image, is showed in Fig. 6.10b from where one may note how the majority of the unstable pixels are detected at the first step. Fig. 6.10c is a 3-D view of the image indices that more influence scatterers time stability at the first step (i.e. discarding one image) and as one may observe from Fig. 6.10d the resulting one is image with ID 6. The trend of the estimated CVm is showed in Fig. 6.11a and the 3-D reconstruction in Fig. 6.11b displays the stable and unstable scatterers in term of the estimated CVm: unstable (orange) pixels, i.e. points with CVm values higher than the estimated threshold, lie mostly on the main skyscraper façades. Focusing on the unstable images, in Fig. 6.10 is represented an example of the time analysis aiming to extract the number and the indices of images that more perturb the 3-D temporally unstable scatterers.
Also the Tour Mirabeau has been taken into account in this analysis. As

[1]The Coefficient of Variation is expressed as the ratio of the standard deviation σ to the mean μ. It is a statistical measure of the dispersion of data points in a data series around the mean, that is the higher the CV the greater the dispersion in the variable. It is an useful statistic for comparing the degree of variation from one data series to another, even if the means are drastically different from each other.

shown in Fig. 6.12 the analysis performed in terms of the CVm reveals that the greater number of the pixel is stable in the time domain. For that the IDs of the unstable images have not been computed.

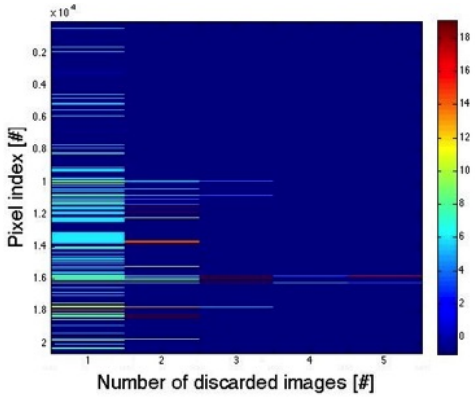

(a) Extraction of the most perturbing contributions

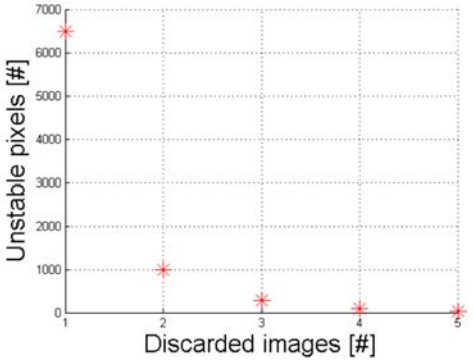

(b) Number of the points at the different steps

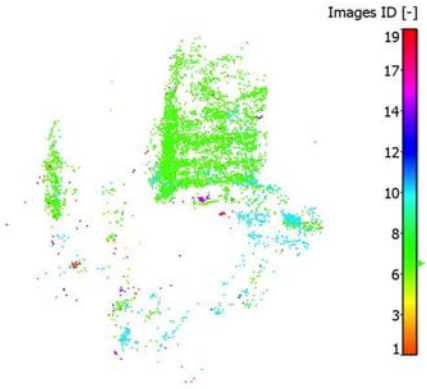

(c) 3-D view: indices at the first step

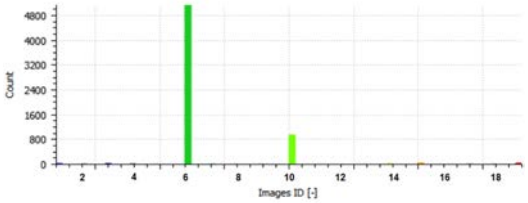

(d) Histogram of the indices at the first step

Fig. 6.10 – Tour Keller area: analysis about the unstable image IDs

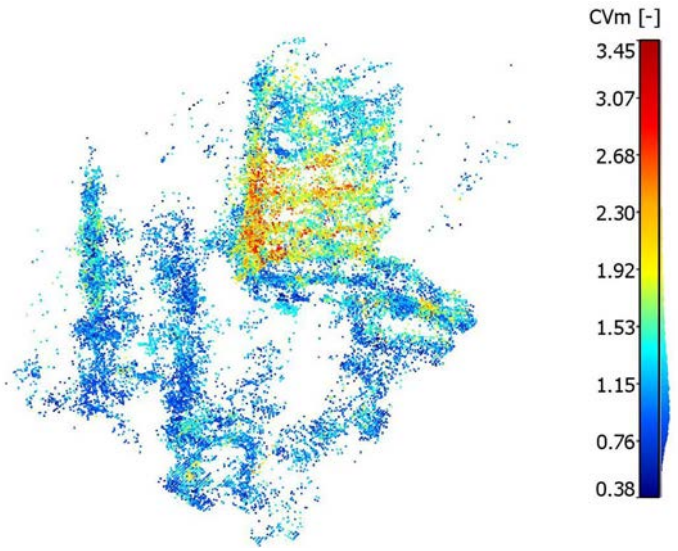

(a) Modified Coefficient of Variation trend

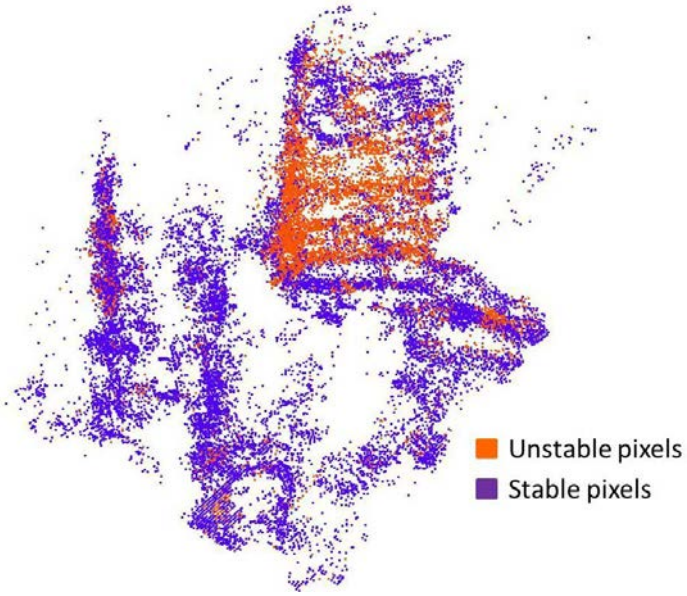

(b) Stable and unstable pixels

Fig. 6.11 – 3-D views of the Tour Keller's area in terms of the CVm

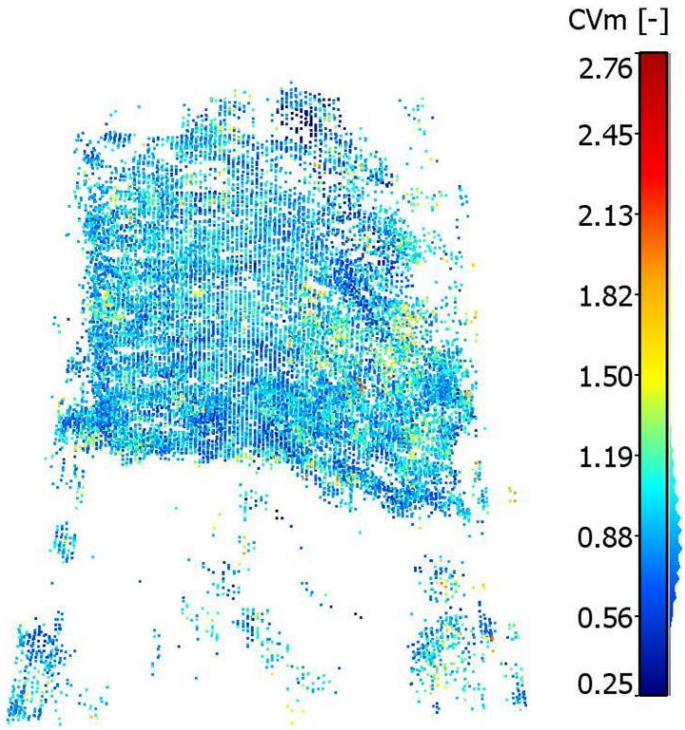

(a) Modified Coefficient of Variation trend

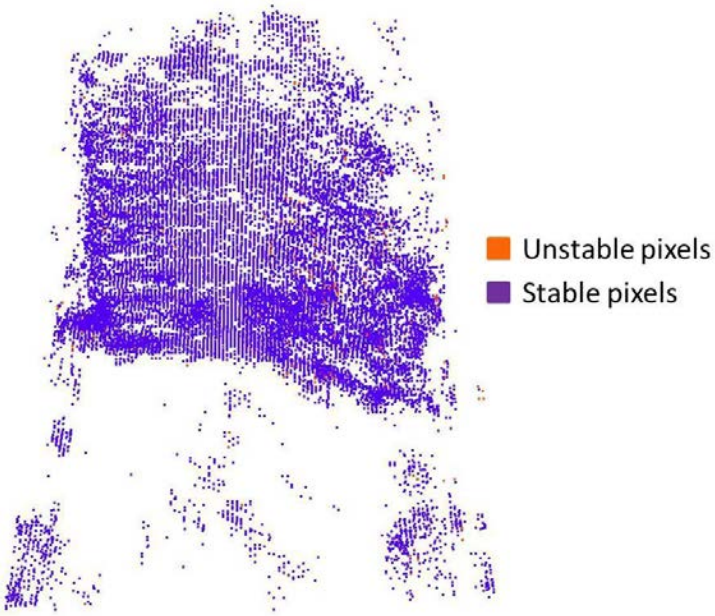

(b) Stable and unstable pixels

Fig. 6.12 – 3-D views of the Tour Mirabeau in terms of the CVm

Chapter 7

Conclusions and outlook

7.1 Conclusions

The main goal of this work was to develop a global and three-dimensional characterization of complex and dense urban areas using tomographic techniques and high resolution satellite SAR imagery. In particular it was taken into account the classical non-parametric and parametric spectral estimation techniques such as the Beamforming, Capon and MUSIC. 2-D and 3-D analysis have been presented over the urban area of Paris acquired by TerraSAR-X sensor in High Resolution SpotLight and Single Polarization mode. The present work is mainly focused on the 3-D reconstruction by very fast estimation techniques and does not take into account parsimonious signal estimators.
In chapter 5 it was underlined the good quality of high resolution SAR data, such as ones acquired by TerraSAR-X, both from the interferometric and time stability and coherence points of view. The analysis of the results and the coherence maps generated over the entire stack allowed to choose the adequate set of multitemporal data to be processed, discarding images considered as outlier in terms of temporal and spatial baselines. Further, the extraction of 2-D tomograms over different azimuth-profile has showed the capabilities to distinguish more than one scatterer within

the same resolution cell and to reconstruct the vertical building profiles. The analysis have regarded the expectation, that is the parametric MUSIC method, respect to the other non-parametric twos, revealed a better sidelobes reduction and accuracy of the estimated products.
Starting from these results the 3-D analysis has been performed in chapter 6 considering different tiles characterized both by mixed features (residential buildings, streets and vegetation) and single skyscrapers inducing a strong layover. The generated point clouds reveal the good reconstruction of building shape and location and a good estimation of their elevation. Indeed, façades intersection, structure features and main streets are well visible from the 3-D reconstruction. Moreover, being able to detect up to three scatterers within the same resolution cell, it has been possible not only to generate more complete point clouds, but also to solve the distortions due to the layover. This has been highlighted for the tile named Tour Keller area, where the second detected sources are mostly related to information lying down the strong layover induced by the tallest skyscraper. The MUSIC approach allowed to detect the highest number of points, especially in the layover cases, and the Capon's results appear to be sparser and noisier respect also to the Beamforming ones.
The analysis performed in terms of vertical reflectivity estimation has led to the identification of strong intensity of the signals at the interaction wall-ground, revealing the double bounce strong reflection occurring in that area. At the same time, the ground is characterized by low reflectivity values.
The most innovative aspect of the present work is represented by the 3-D analysis of the time stability of the detected scatterers. Considering step by step all the images but the one corresponding to the relative step, a set of 3-D intensity have been generated and the stable and unstable scatterers have been distinguished and the IDs of the most perturbing contributions have been found. The study has been developed consider-

ing a modified Coefficient of Variation, respect which the more unstable pixels appeared to belong to the façades of the Tour Keller.
Eventually, it is possible to assert that processing high resolution SAR data allows to achieve a strong improvement in 3-D imaging capabilities. The 3-D reconstructions presented in the present thesis enabled to perform a global characterization of build-up areas, processing an adequate set of multitemporal high resolution SAR images. It has been demonstrated the potentialities of TomoSAR technique in distortions correction, in determining information about the number of scatterers and the corresponding reflectivity within one resolution cell and in 3-D change monitoring using basic mono-dimensional estimators as Beamforming, Capon and MUSIC.
I would like to acknowledge the German Aerospace Centre (DLR) for providing TerraSAR-X data used in this work in the frame of the project ID LAN1746.

7.2 Further investigations and improvements

Even though the inferred conclusions lead to good and encouraging results, there are still interesting issues which may enhance and deepen the developed processing chain. Future investigations should be directed towards improving tomographic technique robustness, refining 3-D change detection and monitoring, studying the integration with other techniques. Summarizing, as main topics one can list:

- *Considering thermal building variations.* In order to enhance the second products quality, it may be interesting to take into account the analysis of the building expansion and contraction due to the thermal loads from exposure to changes in the ambient temperature. Building shape and elevation thermal variations are related

to the local weather patterns along with the heating: warmer materials expand and colder materials contract. This kind of changes, strongly depend on the different temperatures to which the structure is subjected, may occur slowly and may impact the time stability of the detected sources

- *Improving tomographic techniques.* Spectral estimators robustness may be improved applying more sophisticated estimation techniques and a comparison with the Compressive Sensing approach may be performed in order to evaluate the main pros and cons of the two approaches

- *Processing data sets acquired at different spatial resolutions.* Certainly, the processing chain might be applied to other stack(s) representing a complex and dense urban scenarios and acquired both at high and low resolution. An interesting and challenging investigation might be handling Sentinel-1 data, characterized by 5x20m spatial resolution (in Interferometric Wide Swath) and provided by ESA for free and on-line thought the scientific data hub tool. This may lead to study the limits of tomographic techniques respect to the spatial resolution of the precessed data

- *Integration with the Polarimetric SAR.* Polarimetric SAR Tomography (PolTomSAR) is a well-known technique based on the combination of tomograms computed over different polarimetric channels. In this way two different scattering mechanisms could be identified: the single-bounce reflection over rough surface (e.g. ground or building roofs) and the double-bounce reflections characteristic of ground-tree trunk or dihedral-like objects. These different scattering mechanisms, discerned in height direction by tomographic technique, will be used to characterize in a refined way volumetric environments over wide areas and within a very short amount of time. In literature the application of PolTomSAR technique to

urban scenarios by means of SAR satellite data represents an innovative topic and such a technique may be used to retrieve a land cover classification, largely useful tool in different engineering civil application fields. As last goal, all final products could become a valuable tools to supply topographic information in complex environments, in particular urban areas. In this sense a TerraSAR-X proposal project has been successfully submitted and approved and a huge amount of dual polarimetric data stacks, acquired over different AOIs (as Spain, Germany and Japan), is already available to perform the tomographic and polarimetric processing chain

- *DSMs validation.* A DSMs assessment might be performed comparing the extracted DSMs with a more accurate ground truth one, e.g. obtained by means of the LiDAR technology, in order to evaluate their elevation accuracy

References

[1] Earth Snapshot. http://www.eosnap.com/earth-observation/asar-image-orthorectification/. Last access: 10/06/2016. v, 20

[2] F4 3D Map Viewer. `http://demo.f4map.com`. Last access: 08/04/2016. vi, 69, 71

[3] Radar Imaging. http://hosting.soonet.ca/eliris/remotesensing/bl130lec13.html. Last access: 10/06/2016. v, 24, 26

[4] Shuttle Radar Topography Mission (SRTM). https://lta.cr.usgs.gov/SRTM. Last access: 10/06/2016. 40

[5] Wikimedia. https://commons.wikimedia.org/wiki/File:Foreshortening.png. Last access: 10/06/2016. v, 23

[6] Airbus Defence and Space. *TerraSAR-X Image Product Guide. Basic and Enhanced Radar Satellite Imagery*, August 2014. 30

[7] S. Auer, S. Hinz, and R. Bamler. Ray-tracing simulation techniques for understanding high-resolution sar images. *IEEE Transactions on Geoscience and Remote Sensing*, 48(3 PART2):1445–1456, 2010. v, 25

[8] R. Bamler and P. Hartl. Synthetic aperture radar interferometry. *Inverse Problems*, 14(4):r1–r54, 1998. 44, 45

[9] A. Budillon, A. Evangelista, and G. Schirinzi. Three- dimensional sar focusing from multipass signals using compressive sampling. *IEEE Transactions on Geoscience and Remote Sensing*, 49(1):488–499, 2011. 3, 49

[10] E. J. Candès. Compressive sampling. In *Proc. International Congress of Mathematicians*, pages 1433–1452. 50

[11] P. Capaldo, M. Crespi, F. Fratarcangeli, A. Nascetti, F. Pieralice, M. Porfiri, and T. Toutin. DSMs generation from COSMO-SkyMed, Radarsat-2 and TerraSAR-X imagery on Beauport (Canada) test site: Evaluation and comparison of different radargrammetric approaches. volume 40, pages 41–46, 2013. 36

[12] P. Capaldo, F. Fratarcangeli, A. Nascetti, F. Pieralice, M. Porfiri, and M. Crespi. High Resolution Radargrammetry - 3D Terrain Modeling. In D. D. Closson, editor, *Land Applications of Radar Remote Sensing*, chapter 6, pages 167–190. InTech, 2014. 37

[13] P. Capaldo, A. Nascetti, M. Porfiri, F. Pieralice, F. Fratarcangeli, M. Crespi, and T. Toutin. Evaluation and comparison of different radargrammetric approaches for Digital Surface Models generation from COSMO-SkyMed, TerraSAR-X, RADARSAT-2 imagery: Analysis of Beauport (Canada) test site. *ISPRS Journal of Photogrammetry and Remote Sensing*, 100:60–70, 2015. 38

[14] J. Capon. High-Resolution Frequency-Wavenumber Spectrum Analysis. *Proceedings of the IEEE*, 57(8):1408–1418, 1969. 60

[15] J. Curlander and R. N. McDonough. *Synthetic Aperture Radar: Systems and Signal Processing*. Wiley, 1991. 16

[16] A. Ferretti, A. Monti-Guarnieri, C. Prati, and F. Rocca. *InSAR Principles: Guidelines for SAR Interferometry Processing and Interpretation*. ESA, February 2007. 41

[17] A. Ferretti, C. Prati, and F. Rocca. Multibaseline InSAR DEM reconstruction: the wavelet approach. *IEEE Transactions on Geoscience and Remote Sensing*, 37(2 I):705–715, 1999. 40

[18] A. Ferretti, C. Prati, and F. Rocca. Permanent scatterers in SAR interferometry. *IEEE Transactions on Geoscience and Remote Sensing*, 39(1):8–20, 2001. 40

[19] L. Ferro-Famil, Y. Huang, and E. Pottier. Principles and Applications of Polarimetric SAR Tomography for the Characterization of Complex Environments. *International Association of Geodesy Symposia. F. Sanso Ed., Springer-Verlag*, (1-13), Dec. 2015. 49, 54

[20] L. Ferro-Famil and E. Pottier. Urban area remote sensing from L-band PolSAR data using time-frequency techniques. *Urban Remote Sensing Joint Event, URS*, 2007. 49, 75

[21] G. Fornaro, A. Pauciullo, D. Reale, and S. Verde. Multilook SAR Tomography for 3-D Reconstruction and Monitoring of Single Structures Applied to COSMO-SKYMED Data. *IEEE Journal of Selected Topics in Applied Earth Observations and Remote Sensing*, 7(7):2776–2785, July 2014. 50

[22] G. Fornaro, D. Reale, and F. Serafino. Four-Dimensional SAR Imaging for Height Estimation and Monitoring of Single and Double Scatterers. *IEEE Transactions on Geoscience and Remote Sensing*, 47(1):224–237, Jan 2009. 50

[23] G. Fornaro and F. Serafino. Imaging of single and double scatterers in Urban areas via SAR tomography. *IEEE Transactions on Geoscience and Remote Sensing*, 44(12):3497–3505, 2006. 3, 48

[24] G. Fornaro, S. Verde, D. Reale, and A. Pauciullo. CAESAR: An Approach Based on Covariance Matrix Decomposition to Improve

Multibaseline-Multitemporal Interferometric SAR Processing. *IEEE Transactions on Geoscience and Remote Sensing*, 53(4):2050–2065, April 2015. 50

[25] G. Franceschetti and R. Lanari. *Synthetic Aperture Radar Processing*. CRC Press, 1999. 16

[26] P. Gamba, B. Houshmand, and M. Saccani. Detection and extraction of buildings from interferometric SAR data. *IEEE Transactions on Geoscience and Remote Sensing*, 38(1 II):611–618, 2000. 40

[27] F. Gini and F. Lombardini. Multibaseline cross-track SAR interferometry: A signal processing perspective. *IEEE Aerospace and Electronic Systems Magazine*, 20(8 II):71–92, 2005. 57, 60, 63

[28] J. Goodman. Some fundamental properties of speckle. *J. Opt. Soc. Am.*, 66(11):1145–1150, November 1976. 26

[29] L. C. Graham. Synthetic interferometer radar for topographic mapping. *Proceedings of the IEEE*, 62(6):763–768, 1974. 35

[30] J. Homer, I. Longstaff, Z. She, and D. Gray. High resolution 3-D imaging via multi-pass SAR. *IEE Proceedings: Radar, Sonar and Navigation*, 149(1):45–50, 2002. 59

[31] C. Hu, L. Ferro-Famil, and G. Kuang. Ship discrimination using polarimetric SAR data and coherent time-frequency analysis. *Remote Sensing*, 5(12):6899–6920, 2013. 75

[32] Y. Huang and L. Ferro-Famil. 3-D characterization of buildings in a dense urban environment using L-band pol-insar data with irregular baselines. *International Geoscience and Remote Sensing Symposium (IGARSS)*, 3:III29–III32, 2009. 3, 48, 49

[33] Y. Huang, L. Ferro-Famil, and C. Lardeux. Polarimetric SAR tomography of tropical forests at P-Band. pages 1373–1376, 2011. 3, 48

[34] Y. Huang, L. Ferro-Famil, and A. Reigber. Under-foliage object imaging using sar tomography and polarimetric spectral estimators. *IEEE Transactions on Geoscience and Remote Sensing*, 50(6):2213–2225, 2012. 3, 49

[35] D. Johnson and D. Dudgeon. *Array Signal Processing-Concepts and Techniques*, pages 111–190. Prentice Hall, 1992. 59

[36] W. Keller. *Wavelets in geodesy and geodynamics*, pages 11–13, 24–35, 40. Walter de Gruyter, 2004. 28

[37] G. Krieger, A. Moreira, H. Fiedler, I. Hajnsek, M. Werner, M. Younis, and M. Zink. TanDEM-X: A satellite formation for high-resolution SAR interferometry. *IEEE Transactions on Geoscience and Remote Sensing*, 45(11):3317–3340, 2007. 40

[38] D. Kuan, A. Sawchuk, T. Strand, and P. Chavel. Adaptive Restoration of Images with Speckle. *IEEE Transactions on acoustics, speech, and signal processing*, ASSP-35(3):373–383, March 1987. 28

[39] R. Lacoss. Data adaptive spectral analysis methods. *Geophysics,*, 36:134–148, 1971. 60

[40] R. Lanari, O. Mora, M. Manunta, M. J.J., P. Berardino, and E. Sansosti. A small-baseline approach for investigating deformations on full-resolution differential SAR interferograms. *IEEE Transactions on Geoscience and Remote Sensing*, 42(7):1377–1386, 2004. 40

[41] F. W. Leberl. *Radargrammetric image processing.* Norwood, MA : Artech House, 1990. 36, 38

[42] J. Lee. Digital image enhancement and noise filtering by use of local statistics. *IEEE Transaction on pattern analysis and machine intelligence*, PAMI-2(2):165–168, March 1980. 28

[43] J.-S. Lee. A new technique for noise filtering of sar interferometric phase images. *IEEE Transactions on Geoscience and Remote Sensing*, 36(5 PART 1):1456–1465, 1998. 28

[44] M. Mansourpour, M. Rajabi, and J. Blais. Effects and performance of speckle noise reduction filters on active radar and SAR images. *The scientific and technological research council of Turkey*, 2000. 28

[45] D. Massonnet, M. Rossi, C. Carmona, F. Adragna, G. Peltzer, K. Feigl, and T. Rabaute. The displacement field of the Landers earthquake mapped by radar interferometry. *Nature*, 364(6433):138–142, 1993. 40

[46] S. Mèric, F. Fayard, and E. Pottier. Radargrammetric SAR Image Processing. In *Geoscience and Remote Sensing*, chapter 20, pages 421–454. Pei-Gee Peter Ho, 2009. 35, 39

[47] MicroImages, Inc. Introduction to remote sensing with TNTmips®, 2012. 13

[48] A. Nascetti, P. Capaldo, F. Pieralice, M. Porfiri, , F. Fratarcangeli, and M. Crespi. chapter Radargrammetric Digital Surface Models Generation from High Resolution Satellite SAR Imagery: Methodology and Case Studies, pages 1–7. Springer Berlin Heidelberg, Berlin, Heidelberg. 36

[49] A. Nascetti, P. Capaldo, M. Porfiri, F. Pieralice, F. Fratarcangeli, L. Benenati, and M. Crespi. Fast terrain modelling for hydrogeological risk mapping and emergency management: the contribution of high-resolution satellite SAR imagery. *Geomatics, Natural Hazards and Risk*, 6(5-7):554–582, 2015. 39

[50] R. Perko, H. Raggam, J. Deutscher, K. Gutjahr, and M. Schardt. Forest Assessment Using High Resolution SAR Data in X-Band. *Remote Sensing*, 3(4):792–815, 2011. 36

[51] V. F. Pisarenko. The Retrieval of Harmonics from a Covariance Function. *Geophysical Journal of the Royal Astronomical Society*, 33(3):347–366, 1973. 62

[52] M. Porfiri. SAR speckle filtering for radargrammetric Digital Surface Model generation: implementation of several algorithms and analysis of their potentialities. Master's thesis, University of Rome "La Sapienza", October 2012. 28

[53] M. Porfiri, L. Ferro-Famil, and J.-M. Nicolas. Building profile reconstruction using terrasar-x data time-series and tomographic techniques. In *Analysis of Multitemporal Remote Sensing Images (Multi-Temp), 2015 8th International Workshop on the*, pages 1–4, July 2015. 3, 49

[54] B. Rabus, M. Eineder, A. Roth, and R. Bamler. The shuttle radar topography mission - A new class of digital elevation models acquired by spaceborne radar. *ISPRS Journal of Photogrammetry and Remote Sensing*, 57(4):241–262, 2003. 40

[55] D. Reale, G. Fornaro, A. Pauciullo, X. Zhu, and R. Bamler. Tomographic imaging and monitoring of buildings with very high resolution sar data. *IEEE Geoscience and Remote Sensing Letters*, 8(4):661–665, 2011. 3, 49, 50

[56] A. Reigber and A. Moreira. First demonstration of airborne SAR tomography using multibaseline L-band data. *IEEE Transactions on Geoscience and Remote Sensing*, 38(5 I):2142–2152, 2000. vi, 3, 35, 45, 46, 48

[57] S. Sauer, L. Ferro-Famil, A. Reigber, and E. Pottier. Three-Dimensional Imaging and Scattering Mechanism Estimation Over Urban Scenes Using Dual-Baseline Polarimetric InSAR Observations at L-Band. *IEEE Transactions on Geoscience and Remote Sensing*, 49(11):4616–4629, Nov 2011. 49

[58] R. O. Schmidt. Multiple emitter location and signal parameter estimation. *IEEE Transactions on Antennas and Propagation*, AP-34(3):276–280, 1986. 62

[59] P. Stoica and R. Moses. *Spectral Analysis of Signals*, pages 22–37, 159–164, 263–285. Prentice Hall, 2005. 59, 60, 61, 62, 63

[60] S. Tebaldini. Single and multipolarimetric SAR tomography of forested areas: A parametric approach. *IEEE Transactions on Geoscience and Remote Sensing*, 48(5):2375–2387, 2010. 3, 48

[61] S. Tebaldini and L. Ferro-Famil. High resolution three-dimensional imaging of a snowpack from ground-based sar data acquired at X and Ku Band. In *Geoscience and Remote Sensing Symposium (IGARSS), 2013 IEEE International*, pages 77–80, July 2013. 3, 48

[62] S. Tebaldini and F. Rocca. Multibaseline Polarimetric SAR Tomography of a Boreal Forest at P- and L-Bands. *IEEE Transactions on Geoscience and Remote Sensing*, 50(1):232–246, Jan 2012. 3, 48

[63] T. Toutin and R. Chenier. 3-D Radargrammetric modeling of RADARSAT-2 ultrafine mode: Preliminary results of the geometric calibration. *IEEE Geoscience and Remote Sensing Letters*, 6(2):282–286, 2009. 36

[64] T. Toutin and L. Gray. State-of-the-art of elevation extraction from satellite SAR data. *ISPRS Journal of Photogrammetry and Remote Sensing*, 55(1):13–33, 2000. 28

[65] T. Toutin and L. Gray. State-of-the-art of elevation extraction from satellite SAR data. *ISPRS Journal of Photogrammetry & Remote Sensing*, 2000. 42

[66] R. Touzi. A review of speckle filtering in the context of the estimation theory. *IEEE Transaction on geoscience and remote sensing*, 40(11):2392–2404, November 2002. 26

[67] B. Van Veen and K. Buckley. Beamforming: A Versatile Approach to Spatial Filtering. *IEEE ASSP Magazine*, 5(2):4–24, 1988. 59

[68] H. Xie, L. E. Pierce, and F. T. Ulaby. SAR speckle reduction using wavelet denoising and Markov random field modeling. *IEEE Transactions on geoscience and remote sensing*, 40(10):2196–2212, October 2002. 28

[69] H. Zebker, P. Rosen, R. Goldstein, A. Gabriel, and C. Werner. On the derivation of coseismic displacement fields using differential radar interferometry: the Landers earthquake. *Journal of Geophysical Research*, 99(B10):19,617–"19,634", 1994. 40

[70] X. Zhu and R. Bamler. Demonstration of super-resolution for tomographic SAR imaging in urban environment. *IEEE Transactions on Geoscience and Remote Sensing*, 50(8):3150–3157, 2012. 3, 48

[71] X. X. Zhu, N. Adam, R. Brcic, and R. Bamler. Space-borne high resolution SAR tomography: experiments in urban environment using TerraSAR-X Data. In *Urban Remote Sensing Event, 2009 Joint*, pages 1–8, May 2009. 50

[72] X. X. Zhu and R. Bamler. Very High Resolution Spaceborne SAR Tomography in Urban Environment. *IEEE Transactions on Geoscience and Remote Sensing*, 48(12):4296–4308, Dec 2010. 50